A GPR Based Non-destructive Approach to Monitor the Engineering Properties of Compacted Base Layer

Sajib Saha, Ph.D. (Corresponding Author)
Assistant Research Scientist
School of Environmental, Civil, Agricultural, & Mechanical Engineering
University of Georgia
712C Boyd Graduate Center, Athens, GA 30601, US
Email: sajib.saha.ce@gmail.com
ORCID: 0000-0002-1355-4585

Hakan Sahin, Ph.D.
Geotechnical Engineer
Genesis Oil and Gas Consultant Limited
11740 Katy Fwy, Ste 100, Houston, Texas, 77079, US
Email: Hakan.Sahin@genesisoilandgas.com

Narain Hariharan, Ph.D., P.E.
New Products and Applications Engineer – Civil Works
Graymont Limited
585 West Southridge Way, Sandy, Utah 84070, US
Email: nhariharan@graymont.com

Bjorn Birgisson, PH.D., P.E.
Chair, School of Environmental, Civil, Agricultural and Mechanical Engineering
University of Georgia
Boyd Research and Education Center, Athens, GA 30602, US
Email: Bjorn.Birgisson@uga.edu

Robert L. Lytton, Ph.D., P.E., F. ASCE
Professor Emeritus, Zachry Department of Civil and Environmental Engineering
Texas A&M University
Dwight Look Engineering Building, 501F, 3136 TAMU, College Station, Texas, 77843, US
Email: rllytton@mail.com

Peer review status:

This is a non-peer-reviewed preprint submitted to EarthArXiv. The preprint is also submitted to the journal "NDT & E International" for peer review.

ABSTRACT

Construction variability and isolated defects in base layer can be limiting factors in pavement's service life. To control construction quality and implement an efficient quality management system, this study develops a quick, accurate, and simple non-destructive method using ground penetrating radar (GPR) to determine reliable values of in-place compacted base material properties, such as suction (h_m), water content (θ), dry density (γ_d), and resilient modulus (M_R). To overcome the challenges associated with timely laboratory testing on core samples, a set of mechanistic empirical characteristics curve models were utilized and corresponding fitting parameter prediction models were proposed based simple laboratory tests like the Methylene Blue Test (MBT), Percent Size Distribution Analyzer Test, Percometer Test, and Aggregate Imaging Measurement System (AIMS) Test. The laboratory characterization results were integrated with GPR scan data and processed using two GPR signal analysis software programs, PaveCheck and LayerMAPP, to generate a strip map of the in-situ base properties along the pavement section. Finally, to validate the results from the GPR-based approach, the predicted profile of base material properties from filed test sections was compared with results from other non-destructive methods such as the Nuclear Density Gauge and Falling Weight Deflectomter.

Keywords: Ground penetrating radar, non-destructive monitoring, resilient modulus, dry density, pavement layer properties.

1. Introduction

A high-quality base layer, which is applied between the surface layer and the subgrade, provides functional support to the pavement structure and effectively dissipates stresses induced by traffic loads to the underlying subgrade [1]. However, the performance of the base layer can vary significantly depending on construction quality; thus, the properties of the compacted base material should match as closely as possible to those used in the design phase. In current design practices, core samples are extracted from the compacted base layer during construction, and engineering properties are measured in either the laboratory or the field to assess construction quality. A major obstacle in controlling these design properties during construction is the difficulty of collecting core samples and the time-consuming nature of the process. Additionally, construction variability and isolated defects can limit a pavement's service life, and core sample sizes often miss defect areas. Hence, a new approach is needed to efficiently monitor the quality of compacted base material properties in a continuous strip, ensuring high accuracy and precision while minimizing traffic disruptions. This study aims to address this challenge by developing a Ground penetrating radar (GPR) based nondestructive approach integrated with simple and quick laboratory testing protocols for real-time monitoring of engineering properties in the compacted base material. This approach provides a more comprehensive view of pavement layer conditions compared to traditional core sampling methods.

GPR is a nondestructive geophysical tool widely used to detect the properties of the underground layer. It has been adapted and successfully applied by researchers and pavement engineers to predict the characteristics of pavement layer systems. The basic principle of the GPR operation system is that it emits electromagnetic (EM) pulses and receives reflected signals through an antenna, measuring the time of arrival of each wave. The magnitude of the signal amplitudes changes based on the dielectric properties of each layer [2, 3].

In previous research, GPR technology has been widely used to gather information on subsurface layers and determine their properties [4-10]. The variation in water content in most natural soils is considered the principal factor affecting dielectric properties [11]. Consequently, many studies have

assessed water content in base/subgrade layers underlying pavement surface and railways using GPR data [12-14]. A correlation model was established between soil density and GPR survey readings, highlighting that the dielectric permittivity of soils in their natural state depends on water content, which generally decreases as bulk density increases [15]. In a recent study, a GPR-based methodology was proposed to estimate the depth of underlying soil layer as well as soil hydraulic properties [16]. Building on theses previous studies, a methodology was offered for monitoring water content variations in the base layer and evaluating the moisture susceptibility of base aggregate materials through single-offset GPR readings [17].

GPR technology enables high-speed data collection and the analysis of the continuous dielectric profile [18, 19]. A transmitter antenna emits a high-frequency mono-pulse electronic signal, which travels through each layer and reflects at the interface between layers with different dielectric properties. This high-frequency signal is received by the antenna and transmitted to a signal acquisition unit, where it is converted to relatively lower signal pulses. A typical plot of a received radar signal versus arrival time for one pulse is illustrated in Figure 1a. The first amplitude, A_0 reparents the incident wave which emits from the lower end of the antenna. The incident wave reflects at each layer interface, and the reflected waves are plotted as return voltage against their time of arrival in nanoseconds, as shown in Figure 1a. The amplitude, A_1 represents the voltage energy from the surface of pavement, while subsequent amplitudes A_2 and A_3 indicate reflections from the surface of base and subgrade layers, respectively.

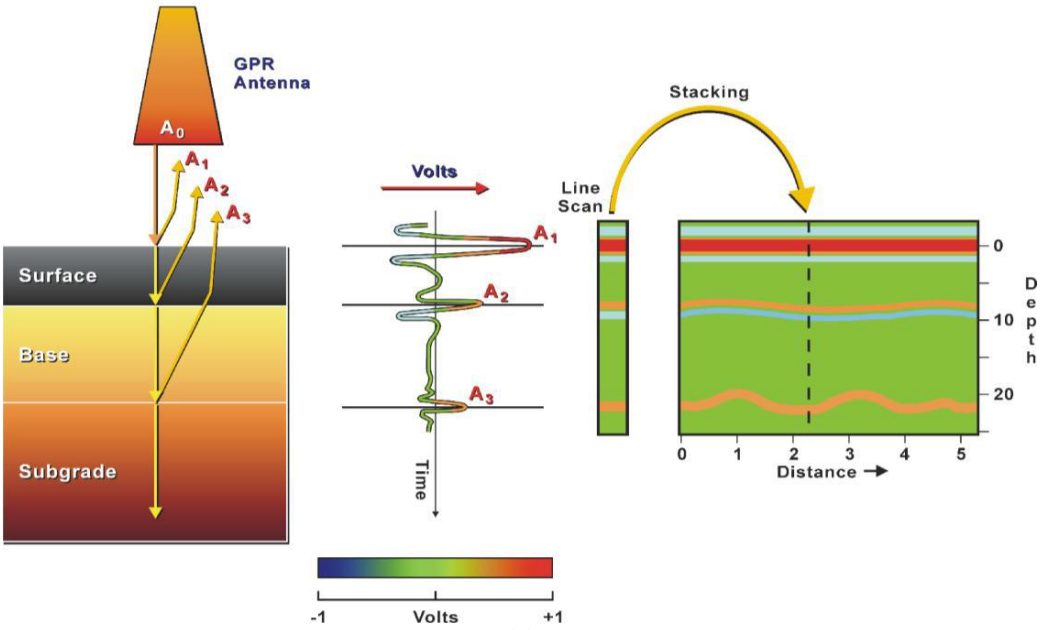

(a)

(b)

Figure 1. (a) Mechanics of signal operation system, and (b) a GPR equipment

These signals are received by a receiver, converted to low frequency, digitized by an A/D converter, and then sent to a host computer for data processing and display. The radar system moves along the survey location, with received waves displayed as a 2-D pseudo-color strip map by the host computer. In this study, an air launched GPR unit was utilized, as shown in Figure 1b. The radar system was carried in a van, with the radar antenna mounted on the front bumper. This particular GPR van can operate at a highway speed of

60 mph while effectively collecting data. It is capable of emitting and receiving 50 pulses per second, penetrating to a depth of 2 feet.

1.1 Principal of Ground Penetrating Radar System

The basic principle of radar wave propagation is that a radar wave traveling through a dielectric medium moves at a velocity (v) equal to the speed of light divided by the square root of the relative dielectric constant, as shown in Equation 1.

$$v = c/\sqrt{\varepsilon} \quad (1)$$

where c = the speed of light (3.0 x 10^8 meters per second) and ε = the relative dielectric constant

When applying the radar wave principle to pavement layer surfaces, the signal is directed vertically downward. As the incident wave (A_0) strikes the pavement surface, a portion of the signal's voltage (A_1) is reflected vertically upward from the surface and the remainder of the electromagnetic energy is transmitted through the surface into the next layer, as depicted in Figure 1a. The transmitted wave encounters the next interface between layers (surface and base) with different dielectric constants, resulting in another reflection (A_2) and transmission voltage. This process continues as the wave reflects off the base-subgrade interface and travels back to the surface, undergoing further reflections and transmissions at each layer interface. Each pavement layer interface has a reflection and a transmission coefficient. The reflection coefficient for any interface between layer i and layer $i+1$ can be expressed as a function of the relative dielectric properties (ε) of the adjacent layers.

$$\rho_{i,i+1} = \frac{\sqrt{\varepsilon_{i+1}}-\sqrt{\varepsilon_i}}{\sqrt{\varepsilon_{i+1}}+\sqrt{\varepsilon_i}} \quad (2)$$

The corresponding transmission coefficient is expressed in Equation 3.

$$T_{i,i+1} = 1 + \rho_{i,i+1} \quad (3)$$

As the radar wave strikes the pavement surface or layer interfaces, the amplitudes of the reflected and transmitted waves are diminished. The amplitude of the incidence wave (A_0) and the reflected wave

(A_1) from the surface are related through the reflection coefficient (ρ_{01}) for the pavement surface, as shown in Equation 4.

$$A_1 = A_0 * \rho_{01} \quad (4)$$

Similarly, the amplitude of the reflected wave (A_2) from the surface-base layer interface is related to the incident wave amplitude (A_0), as shown in Equation 5.

$$A_2 = (A_0 * T_{01}) * \rho_{12} * T_{10} \quad (5)$$

By measuring the amplitudes of each reflected wave, the reflection coefficient, ρ_{01}, in Equation 4 can be replaced with Equation 2 to calculate the dielectric constant, ε_1, of the surface layer.

$$\varepsilon_1 = \left[\frac{1+\frac{A_1}{A_0}}{1-\frac{A_1}{A_0}}\right]^2 \quad (6)$$

The amplitude of the incident wave, A_0, can be determined by measuring the amplitude of the reflection wave from a large metal plate (represents the case of 100% reflection).

Equations 2, 3, 5, and 6 can be employed to determine the relative dielectric constant of the base layer, ε_2.

$$\varepsilon_2 = \varepsilon_1 \left[\frac{1-(\frac{A_1}{A_0})^2+(\frac{A_2}{A_0})}{1-(\frac{A_1}{A_2})^2-(\frac{A_2}{A_0})}\right]^2 \quad (7)$$

Additionally, the arrival times of each reflected wave are also measured (in nanoseconds) and the time interval between the arrivals of reflected waves, Δt_i , is used to determine the thickness, h_i, of each layer using Equation 8.

$$h_i = \frac{c*\Delta t_i}{2\sqrt{\varepsilon_i}} \quad (8)$$

Hence, the thickness of the surface layer and the base layer can be estimated following Equation 9.

$$h_1 = \frac{c*\Delta t_1}{2\sqrt{\varepsilon_1}}; \text{ and } h_2 = \frac{c*\Delta t_2}{2\sqrt{\varepsilon_2}} \quad (9)$$

where h_1 and h_2 yield the thickness of the surface and base layers respectively, c is the speed of the electromagnetic wave in air (5.9 inches/ nanosecond for two-way travel), Δt_1 is time delay (in nanoseconds) between A_1 and A_2, and, Δt_2 is time delay (in nanoseconds) between A_2 and A_3. In this study, the thickness

(h_2) and dielectric constant (ε_2) values of the base layer were processed as a continuous strip along the GPR survey path using the PaveCheck software program. The focus of this study is to integrate GPR scan data with simple laboratory characterization test results to determine reliable values of the in-place as compacted base material properties. The key objectives are described below.

- Experimental characterization of base engineering properties i.e., suction (h_m), water content (θ), dry density (γ_d), resilient modulus (M_R) for the collected aggregate materials
- Development of a set of characteristics curves, i.e., the soil-water characteristic curve (SWCC), suction-dielectric characteristic curve (SDCC), compaction curve model (CCM) based on experimental test results
- Development of a set of correlation models to predict fitting parameters for characteristics curves based on simple base course properties, including the Methylene Blue Value (*MBV*), percent fine content (*pfc*), dielectric constant (ε), and the angularity (A), shape (S), and texture (T) characteristics of the base materials
- To implement the GPR-based monitoring approach by integrating GPR scan data with laboratory characterization curves to estimate the base material properties for two field pavement sections
- To validate the GPR predicted base material properties using other nondestructive testing approaches i.e., Falling Weight Deflectometer (FWD), Nuclear Density Gauge.

2. Methodology

Figure 2 illustrates the procedures for implementing the GPR-based mechanistic-empirical approach in field projects. The outputs from the GPR scan are analyzed using the software program PaveSCM to obtain the dielectric constant profile of base layer. The generated characterization curves (SDCC, SDCC, CCM) for the base materials derived from laboratory characterization test results, and dielectric constant data, are then input into the software program LayerMAPP. The program analyzes this information to estimate the engineering properties of in-situ compacted base layer, including suction (h_m), water content (θ), dry

density (γ_d). The estimated values for h_m, θ, and coefficient of resilient modulus (M_R) are subsequently entered into a built-in Finite Element Program (FEM) to determine the M_R value based on a stress- and-water content sensitive M_R-model. To validate the GPR-based nondestructive approach, the predicted values of θ, γ_d, and M_R for the base layer from filed projects are compared to those obtained from other non-destructive methods such as Nuclear Density Gauge readings and backcalculated FWD test data.

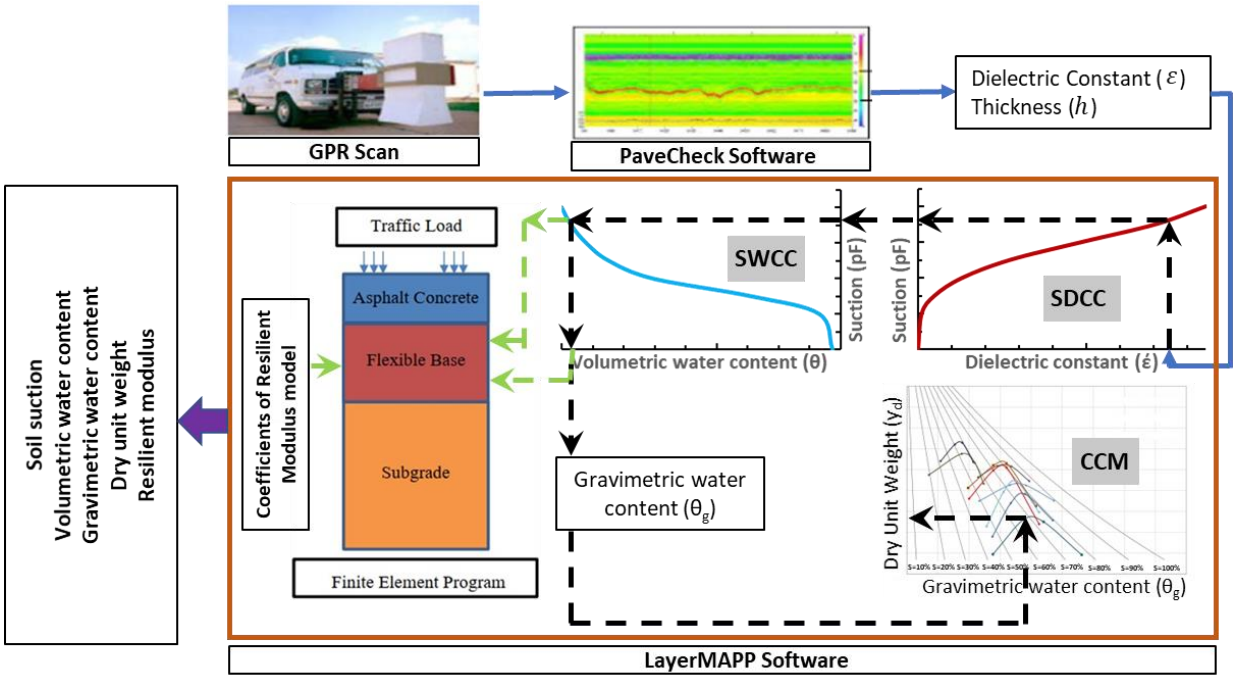

Figure 2. A Schematic flow chart presenting the process estimating base properties using GPR approach

3. Laboratory Test Results

To experimentally characterize and validate prediction models for engineering properties, i.e., suction (h_m), water content (θ), dry density (γ_d), and resilient modulus (M_R), base aggregate samples were collected from nine quarries across Texas. The laboratory tests conducted include the filter paper test to determine suction, the compaction test to measure dry density at specific water content, and the resilient modulus test to determine the base modulus value. The following subsections provide a detailed description of these tests, including the test protocols, procedures, and results.

3.1. Soil Suction (Filter Paper Test)

The filter paper test is widely used as a standard method for measuring soil suction in unsaturated soil mechanics. In this study, the filter paper test procedure was employed to measure the matric suction (h_m) of aggregate materials passing through the No.4 sieve.

3.1.1. Filter Paper Test Procedure

Two compacted aggregate specimens were prepared for each type of base material using the standard compaction method outlined in ASTM D 698 [20]. The size of the compacted specimens was 1.5 in. in height and 3 in. in diameter. The compacted soil specimens were kept in a 100 percent humidity room until they dried down to a desired water content level. Once the samples reached the desired water content, they were taken out the environmental room and immediately placed for the filter paper test. One filter paper was placed between two compacted specimens to measure matric suction, while two additional filter papers were placed on top of the sample to measure the total suction. The specimens were then placed in a jar and sealed with electrical tape. These specimens were kept for 7 days in the sealed jar. After 7 days, the water content in filter papers and the corresponding suction level in the specimens would reach an equivalent phase. The jar was opened afterward, and the suction values were determined by weighing the water content of the filter papers using a highly accurate scientific scale. The filter paper test procedure is described in ASTM D5298 [21]. The complete testing protocol for a compacted base aggregate sample is illustrated in Figure 3.

3.1.2. Filter Paper Test Results

The moisture content absorbed by the filter paper is converted into a suction value based on a calibration curve [22]. The suction values were recorded in log *kPa* units, where the suction in log *kPa* equals $\log_{10}$ |suction in *kPa*|. Table 1 lists the measured suction values for the collected base materials in kPa units.

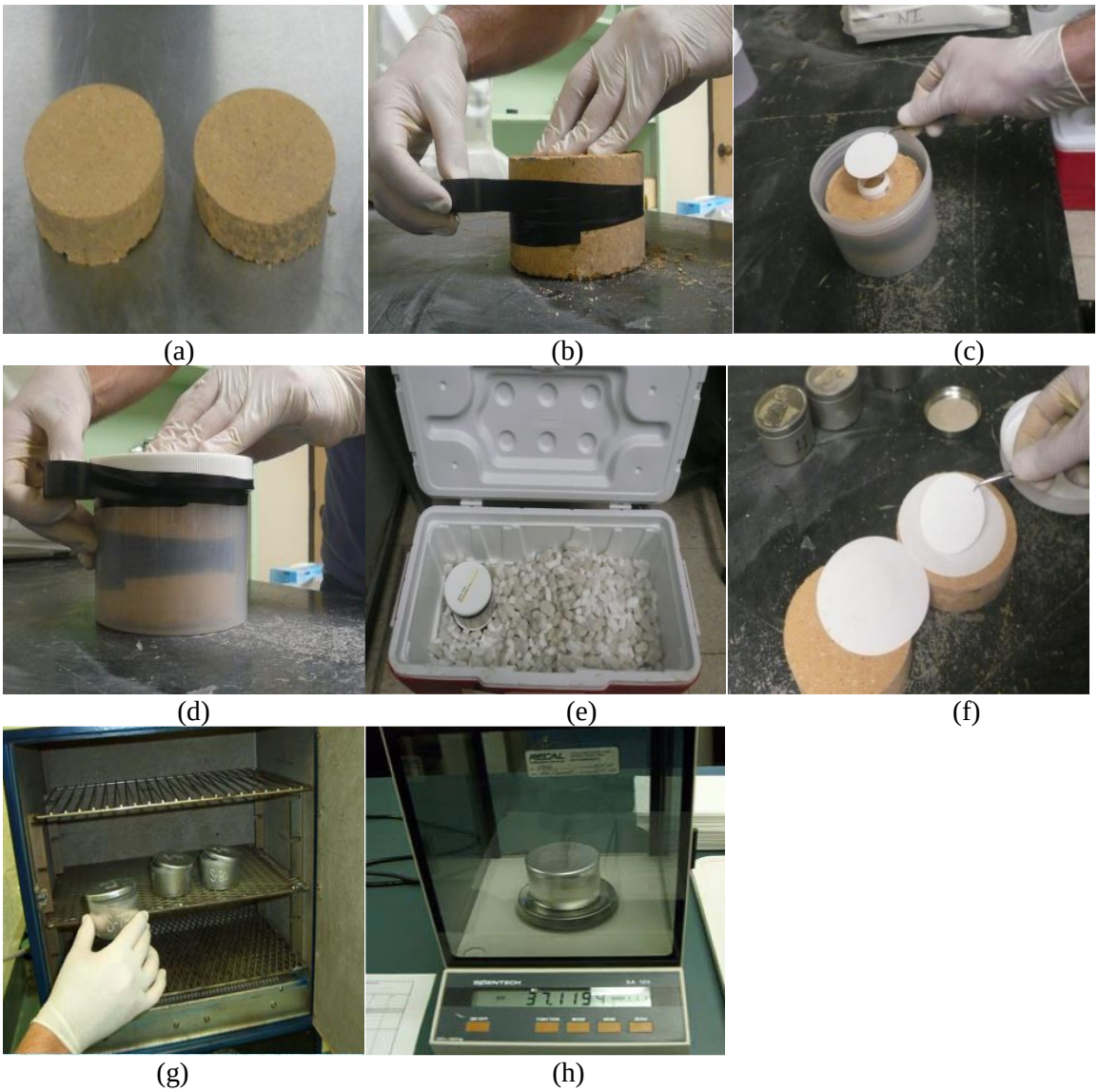

Figure 3. Filter Paper suction test procedure steps (a) compacted identical base aggregate specimens, (b) one filter paper in between two specimens, (c) two filter papers placed on top of a plastic ring, (d) the process of placing specimens in a jar and sealing it, (e) storing the sealed jar in a chest box, (f) after equilibrium period, opened the seal jar and weigh the wet filter papers along with the tin, (g) placing the tin with wet the filter paper in a hot oven, and (d) weigh the tins along with the dry paper

Table 1. Measured suction values for collected aggregate materials

Source material	Volumetric water content, θ_v (%)	Matric Suction, h_m (kPa)		Source material	Volumetric water content, θ_v (%)	Matric Suction, h_m (kPa)	
		Mean value	SD			Mean value	SD
E-01	4.0	-50.1	0.3	E-06	4.0	-125.9	0.6
E-02	4.1	-39.8	0.3	E-07	4.3	-63.1	0.3
E-03	4.1	-20	0.8	E-08	4.1	-63.1	0.2
E-04	3.9	-100	1.1	E-09	4.0	-63.1	0.2
E-05	4.2	-100	0.2				

3.2. Dry Density (Compaction Test)

Since the base materials are three-phase mixtures consisting of solid particles, water, and air, the relative amounts and arrangement of these components have considerable effects on the physical and mechanical properties of the materials [23]. In construction, compaction is a necessary process that involves applying energy to the materials to rearrange these three phases, which results in increased density and strength. The two essential factors in quality control of base material compaction are water content (θ) and dry density (γ_d) [24, 25]. The standard test procedure was followed in this study to perform compaction tests on each collected sample, aiming to establish the water-density relationship of the base materials [26].

3.2.1. Compaction Test Procedure

The base materials were compacted in a mold measuring 6 inches (152.4 mm) in diameter and 8 inches (203.2 mm) in height. The materials were molded in four layers using a 10 lb. (4.53 kg) rammer. The rammer was dropped from a height of 18 $\pm$ 1/2 inches (457 $\pm$ 12.7 mm) until a total compaction energy of 750.0 ft-lbs was delivered equally to each layer, as measured by the soil compactor analyzer (SCA) device. To achieve the energy, a total of 50 $\pm$ 5 drops was applied. This test procedure involved using aggregate that passed through the 1-3/4 in. (45 mm) sieve, followed by the use of a 7/8 in. (22.6 mm) sieve to separate the aggregate retained on the 7/8 in. sieve from the aggregate that passed through it. The separated materials- both retained and passing through the 7/8 in. sieve- were distributed equally based on size, shape, and quantity into four separate layers. This process was repeated five times with varying moisture contents to obtain a well-defined water content versus dry density curve.

Figure 4. Compaction equipment used for molding a specimen with SCA

3.2.2. Compaction Test Results

After compaction, the gravimetric water content of the specimen was determined by measuring the difference in weight. The wet density was calculated by dividing the wet mass by the volume of the mold used. Next, the dry density was computed using the wet density (γ_w) and the gravimetric water content (θ_g), according to Equation 10.

$$\gamma_d = \frac{\gamma_w}{1+\theta_g} \tag{10}$$

This process was repeated five times for each aggregate source, with the water content being increased after each iteration and the corresponding dry density calculated. The dry densities calculated for the tested water contents of each aggregate source are listed in Table 2.

Table 2. Compaction test results for each pit at five different water contents

Source material	Gravimetric water content, θ_g (%)					Dry density, γ_{dry} (pcf)				
E-01	3.92	4.78	5.58	5.80	6.37	139.60	141.84	143.16	143.00	142.63
E-02	5.81	6.65	7.10	7.61	8.15	135.00	137.00	137.10	136.63	135.78
E-03	7.09	7.60	8.04	9.04	9.68	130.28	130.80	130.92	128.63	126.39
E-04	4.13	4.95	5.78	6.00	6.60	134.41	137.98	143.62	142.10	140.55
E-05	4.66	5.58	6.00	6.41	6.77	131.01	140.63	141.50	140.18	138.97
E-06	4.12	4.98	5.60	5.89	6.64	144.06	149.72	150.40	149.63	147.72
E-07	6.06	6.80	7.40	7.55	8.41	132.69	136.69	137.70	137.68	134.71

E-08	5.03	5.72	6.50	6.58	7.69	143.33	144.34	145.80	146.29	143.60
E-09	6.31	6.90	7.32	7.85	9.11	132.50	135.40	136.44	135.83	134.28

3.3. Resilient Modulus Test

The resilient modulus of unbound aggregates is widely used to describe the response of the base layer under traffic loads. It is defined as the ratio of the maximum cyclic stress to the recoverable resilient strain in one repeated dynamic loading cycle. In this study a Repeated-Load Triaxial (RLT) test was conducted on cylindrical aggregate specimens using a triaxial chamber equipped with a closed-loop test system.

3.3.1. Resilient Modulus Test Procedure

In order to consider the cross-anisotropic behavior of unbound aggregates, a new loading protocol has been developed to determine the actual responses of aggregate layers under various types of traffic loading [27]. For each loading sequence, the specimens were tested at a constant confining pressure and an axial cyclic stress applied in a haversine waveform, with a load duration of 0.1 seconds and a cycle duration of 1.0 seconds.

Base aggregate specimens were prepared using a vibratory compaction machine as recommended in the AASHTO sampling protocol [28]. These granular specimens were compacted at a specific moisture content and corresponding densities. The dimensions of the specimens were 6 inches diameter and 12 inches in height. After de-molding, each specimen was wrapped in a plastic membrane to minimize moisture loss and was kept for 14 hours, or overnight, to allow the water inside the specimen to distribute uniformly. One linear variable differential transformer (LVDT) was attached to each side of the specimen before being placed into the triaxial chamber. The gauge length of LVDTs, used to compute strain, was 6 inches. Figure 5 shows the specimen with LVDTs attached before the repeated loading test started. Figure 5b illustrates the configuration of the resilient modulus test. Prior to the test, the pressure inside the chamber was increased until it reached the desired confining pressure. Then, the axial load was applied to the specimen through the loading frame in the Material Testing System (MTS). The entire testing process was controlled by a computer program that specified both the axial load and the confining pressure. During each test, two

LVDTs measured the vertical deformations of the specimen. The loading and deformation test data were analyzed to assess the recoverable and unrecoverable behavior of the granular base material.

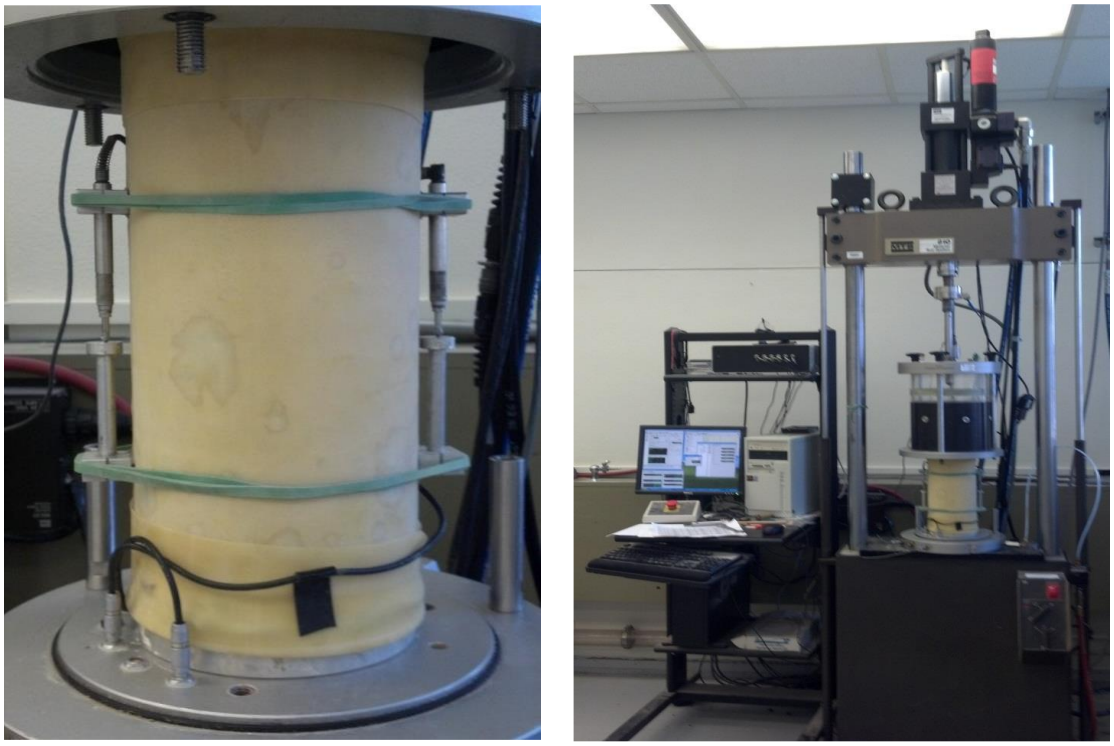

(a) (b)

Figure 5. (a) Sample preparation before resilient modulus test; (b) configuration of Material Testing System (MTS) test machine with a mounted specimen

3.3.2. Resilient Modulus Test Results

The resilient modulus (M_R) value of the aggregate specimen was measured for each loading sequence. Since aggregate base material is both stress and water-content dependent, it is necessary to predict the M_R-value at any specific stress and water-content level. In this study, a modified M_R model was used to consider the influence of water content, suction, and stress on M_R characteristics [29]. The model used is presented in Equation 11.

$$M_R = k_1 P_a \left(\frac{I_1 - 3*\theta_v * f * h_m}{P_a}\right)^{k_2} \left(\frac{\tau_{oct}}{P_a}\right)^{k_3} \quad (11)$$

where I_1 is the first invariant of the stress tensor, P_a is the atmospheric pressure, θ_v represents the volumetric water content, h_m is the matric suction in the aggregate matrix, f is the saturation factor, $1 \leq f \leq \frac{1}{\theta}$, τ_{oct}

is the octahedral shear stress, and k_1 , k_2, and k_3 are fitting parameters that dependent on the aggregate material properties. Table 3 presents examples of the resilient modulus test results for all aggregate samples tested at optimum moisture content, under a confining pressure of 7 psi and a deviatoric stress of 20 psi.

Table 3. Resilient modulus test results for aggregate specimen at specific water content

Source material	Volumetric water content,θ	Matric Suction, h_m (kPa)	k_1	k_2	k_3	Resilient Modulus (M_R) (MPa)
E-01	0.133	-63.1	2440.2	0.36	0.00	368.88
E-02	0.155	-100	299.2	1.05	-0.07	107.87
E-03	0.161	-316.2	773.9	0.74	-0.10	241.20
E-04	0.136	-79.4	544	1.21	-0.12	229.37
E-05	0.136	-41	772.4	1.25	-0.14	322.71
E-06	0.135	-39.8	1198.2	0.84	-0.02	303.83
E-07	0.163	-63.1	456.7	1.21	-0.12	191.53
E-08	0.152	-39.8	1464.5	0.78	-0.05	354.55
E-09	0.173	-63.1	1206	0.87	-0.03	332.56

4. Characteristics Curves to Determine the Base Properties

This study aims to establish a quick, accurate, and straightforward method for determining reliable values of the engineering properties of compacted base materials using radar scan data. To achieve this, a set of characteristic curves and a model were utilized, such as the soil-water characteristic curve (SWCC), the suction-dielectric characteristic curve (SDCC), the compaction curve, and a resilient modulus (M_R) model. Typically, generating these characteristic curves requires a special set of laboratory equipment, experienced labor, and extensive testing schedules. For instance, laboratory procedures such as pressure plate or filter paper tests can take two days to a week to measure suction values and subsequently generate the SWCC. To eliminate the challenges associated with laboratory testing, this study utilized more easily determined soil properties as an efficient alternative for predicting the characteristic curves. The series of tests to determine these soil properties include: (1) the methylene blue test to determine the methylene blue value (MBV), (2) the Horiba particle size distribution analyzer test to determine the percent fines content (pfc), (3) the percometer test to measure the dielectric constant value, and (4) the aggregate imaging measurement system (AIMS) test to measure the geometric characteristics (angularity, shape, and texture) of the base material. The methylene blue value (MBV) assesses the amount of percent clays, a key factor influencing

the relationship between soil suction and moisture content. The dielectric constant value and percent fine content (pfc) are related to the suction value (based on corresponding water content) and the total amount of specific surface area, respectively, helping to generate a unique suction-dielectric constant relationship. The dry density-moisture content relationship, represented by the compaction curve model (CCM), is established using a co-relationship with MBV, pfc, and specific gravity (G_S). Finally, to predict the coefficients of the resilient modulus model, the *k*-values were correlated with simple base course properties, including the dry density (γ_d), pfc, and aggregate geometric characteristics such as gradation, angularity, shape, and texture.

4.1. Methylene Blue Test

The W. R. Grace methylene blue test is widely used to establish a direct relationship between the clay content and the MBV for a wide range of soil types. MBV measures the clay content based on the fact that the negative charges on the clay particle surfaces can have ion exchanges with methylene blue cations, which brightens the methylene blue solution [30-32]. The W.R. Grace test protocol was modified at Texas A&M University to enable its use for the detection of both non-plastic and plastic fines from soils [33]. The fines are classified as non-plastic and plastic materials according to their different specific surface area. The Methylene Blue separates these two types of fines at the critical value of 7.00 mg/g. A detailed description of the methylene blue test procedure and generation of SWCC for unbound aggregate materials based on the test results was presented in a previously published paper [34].

As shown in Figure 6, the methylene blue test apparatus consists of a colorimeter, a timer, a 45 mL plastic tube, a 500-microliter micropipette tip, a syringe, a 0.20 micrometer size filter, an eye-dropper, a 1.4 mL small plastic tube, a portable scale, distilled water, and methylene blue solution. Table 4 lists the results of the methylene blue tests for the selected base materials.

Table 4. Methylene blue values for the selected aggregates

Material source	MBV (mg/g)	Material source	MBV (mg/g)
E-01	4.96	E-06	7.12
E-02	5.32	E-07	7.04
E-03	18.50	E-08	6.76
E-04	16.36	E-09	3.11
E-05	2.41		

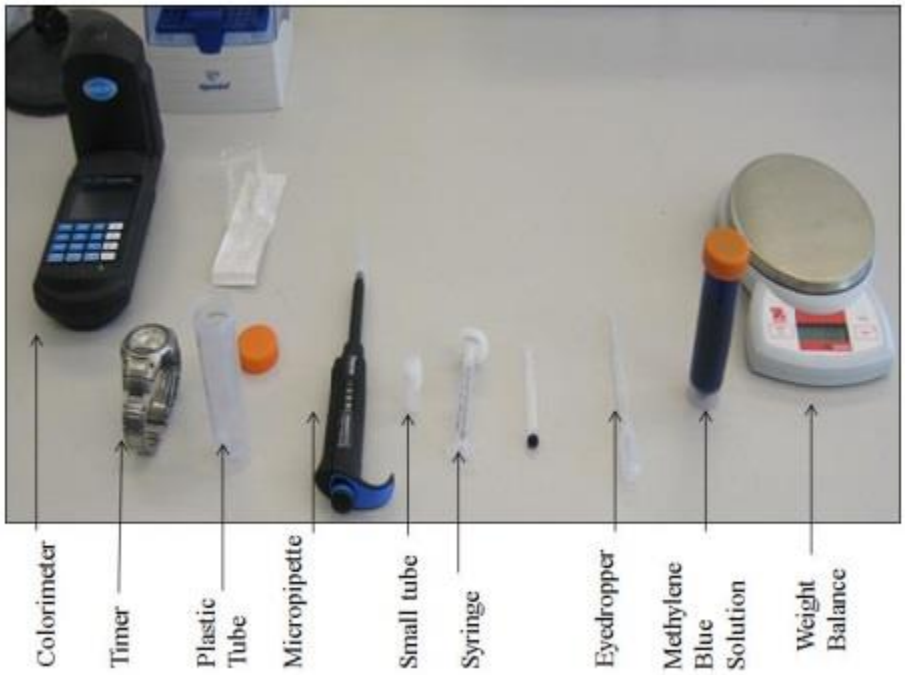

Figure 6. Configuration of Methylene Blue Test

4.2. Particle Size Distribution Analyzer Test

A Horiba laser-scattering, particle-size distribution analyzer was used in this study to determine the pfc of aggregates, which is shown in Figure 7. In the particle size distribution test, a viscous solution made of the particles that pass through a No. 200 sieve and water is passed through a beam of light. As different sizes of particles scatter light at different angles, the percentage of the particles smaller than $2\mu m$ can be determined by analyzing the intensity of the scattered light at certain angles. The light scattering device analyzes the dimensions of various particles in the solution and generates a particle size distribution ranging from the smallest to the largest particle size.

Figure 7. HORIBA LA-960 Laser Particle Size Analyzer

The *pfc* is calculated according to Equation 12.

$$\text{Percent Fines Content } (pfc) = \frac{m_{2\mu m}}{m_{75\mu m}} \quad (12)$$

where $m_{2\mu m}$ is the mass of aggregate smaller than 2 microns, and $m_{75\mu m}$ is the mass of aggregate smaller than 75 microns.

Table 5 shows the *pfc* of the test samples.

Table 5. Percent fines content (pfc) values for aggregates

Material source	*pfc* (%)	Material source	*pfc* (%)
E-01	16.10	E-06	13.20
E-02	11.43	E-07	15.48
E-03	22.83	E-08	13.55
E-04	12.71	E-09	13.25
E-05	22.20		

4.3. Percometer Test

The Percometer test is a fast and nondestructive method to measure the dielectric constant and electrical conductivity of base materials, both in the laboratory and during in-situ testing [33, 35]. Figure 8 shows the standard Adek Percometer equipped with a surface probe while taking measurements on cylindrical specimens. The cylindrical specimens that were prepared for filter paper tests were used for Percometer measurements.

Figure 8. Adek Percometer measuring the dielectric constant of compacted base samples

Dielectric constant measurements were taken immediately before starting the filter paper test to ensure that suction and dielectric constant were measured at the same moisture level. The readings were carefully taken from five different points on the surface of each specimen. The mean value and standard deviation of the collected measurement for each base material is presented in Table 6.

Table 6. Measured dielectric constant values of collected aggregate materials using Percometer device

Source material	Volumetric water content, θ_v (%)	Dielectric Constant, ε_r	
		Mean value	SD
E-01	4.0	-50.1	0.3
E-02	4.1	33.0	0.3
E-03	4.1	24.0	0.8
E-04	3.9	14.0	1.1
E-05	4.2	12.5	0.2
E-06	4.0	15.0	0.6
E-07	4.3	12.0	0.3
E-08	4.1	9.5	0.2
E-09	4.0	10.1	0.2

4.4. Aggregate Imaging Measurement System Test

The Aggregate Image Measurement System (AIMS) is a computer-integrated laboratory test device that analyzes morphology of aggregates, including shape, angularity, and surface texture [36]. It is comprised of a computer, image acquisition hardware, a high-resolution camera, a microscope, an aggregate tray, and a lighting system, as shown in Figure 9. Aggregate shape characterizes the flatness and elongation of aggregate particles, angularity evaluates the degree of roundness of aggregate corners, and surface texture

defines the roughness of aggregate surfaces. In this study, coarse aggregate particles collected from nine different quarries were tested using the AIMS device. The washed coarse aggregates were separated first by retaining materials on 1/2 in., 3/8 in., and No. 4 sieves. The materials retained on each sieve were placed in the aggregate tray and scanned by the high-resolution camera. A detailed description of the AIMS test procedure and distributions of the measured indices for angularity, shape, and surface texture, was presented in a previously published article [27].

Figure 9. (a) Aggregate Imaging Measurement System (AIMS) Test device; (b) AIMS Camera System

In order to quantify the test results, a known statistical distribution was fitted to the distributions measured from the AIMS test. The cumulative Weibull distribution function was adopted in this study as shown in Equation 13.

$$F(x; a, \lambda) = 1 - e^{-\left(\frac{x}{\lambda}\right)^{a}} \quad (13)$$

where $F(x; a, \lambda)$ is the cumulative probability; x is the composite angularity, shape, or surface texture indices; λ is the scale parameter; and a is the shape parameter [37]. The determined shape parameter a and scale parameter λ were used to quantify the AIMS test results. Table 7 presents the fitted cumulative Weibull distribution parameters for the collected base samples. The subscripts in Table 7 denote the following: G is for gradation, A is for angularity, S is for shape, and T is for texture.

Table 7. Cumulative Weibull distribution parameters of aggregate materials

Source material	Gradation		Angularity		Shape		Texture	
	a_G	λ_G	a_A	λ_A	a_S	λ_S	a_T	λ_T
E-01	0.8783	8.31	4.38	3336.93	4.66	8.19	3.16	287.58
E-02	0.8663	14.57	5.09	3113.11	4.11	8.56	2.51	194.07
E-03	0.747	9.859	3.25	3633.44	4.27	8.15	2.87	253.88
E-04	0.98	12.2	5.1	3072.87	3.65	8.03	1.96	171.51
E-05	0.7	10	3.79	3291.5	3.96	7.75	2.12	165.78
E-06	0.6652	9.585	4.76	3327.99	4.44	8.86	2.93	174.63
E-07	0.8467	12.69	4.53	3210.45	4.63	7.97	1.86	138.83
E-08	0.884	10.81	4.99	3342.81	3.63	8.72	1.48	205.58
E-09	0.9048	11.33	3.75	3228.12	4.48	7.6	1.75	205.47

4.5. Soil-Water Characteristics Curve (SWCC) Prediction Model

There are two popular approaches to determining the SWCC for an unbound base material: (1) experimental methods such as filter paper or pressure plate test where suction values are measured at different moisture contents, (2) estimation of the fitting parameters of the Fredlund and Xing SWCC equation, as shown in Equations (14) and (15) [38].

$$\theta_v = C(h)x[\frac{\theta_{sat}}{\{\ln[e+(\frac{h}{a_f})b_f]\}^{c_f}}] \quad (14)$$

$$C(h) = [1 - \frac{ln(1+\frac{h}{h_r})}{ln(1+\frac{1x10^6}{h_r})}] \quad (15)$$

where θ_v = volumetric water content; θ_{sat} = saturated volumetric water content; h = matric suction; and a_f, b_f, c_f, and h_r = fitting parameters.

The four-fitting parameters, a_f, b_f, c_f, and h_r, can be used to determine the suction value at any water content, thereby establishing the SWCC for a specific soil type [39, 40]. Several research studies have correlated these fitting parameters with the weight percent of material passing sieve No. 200 (P_{200}), effective grain size with 60% passing weight (D_{60}), and plasticity index (PI) [41-43]. However, the predictive variables, including P_{200} and PI, demonstrate significant variability [44]. Hence, The SWCCs generated based on these variables also possess considerable variability compared to the measured SWCCs. Given

this circumstance, this study employed a methylene blue value (MBV)-based estimation method proposed by Sahin [33]. Test results and findings from previous research indicate that the four SWCC fitting parameters primarily depend upon gradation and clay content of the soil. The MBV also assess the fine clay content in the unbound aggregate material.

To investigate the correlation between the four SWCC fitting parameters and the MBV, two critical steps were followed. The first step involved determining the four parameters based on the experimental data using the curve fitting method. The second step was to establish the relationships between these parameters and the MBV through regression analysis. Each fitting parameter shows a unique relationship with the MBV, which is presented in Equations 16-19.

$$a_f(psi) = 3.4994 * MBV^{0.0002} \quad (16)$$

$$b_f = 2.0044 * MBV^{-0.003} \quad (17)$$

$$c_f = 0.4956 * MBV^{-0.415} \quad (18)$$

$$h_r(psi) = 20.00 * MBV^{9.5E-06} \quad (19)$$

In addition to these correlation equations, Figure 10 shows that there is good agreement between the fitting parameters and the MBV. Hence, this approach allows for the prediction of the SWCC for any unbound base material by calculating the fitting parameters based on the MBV.

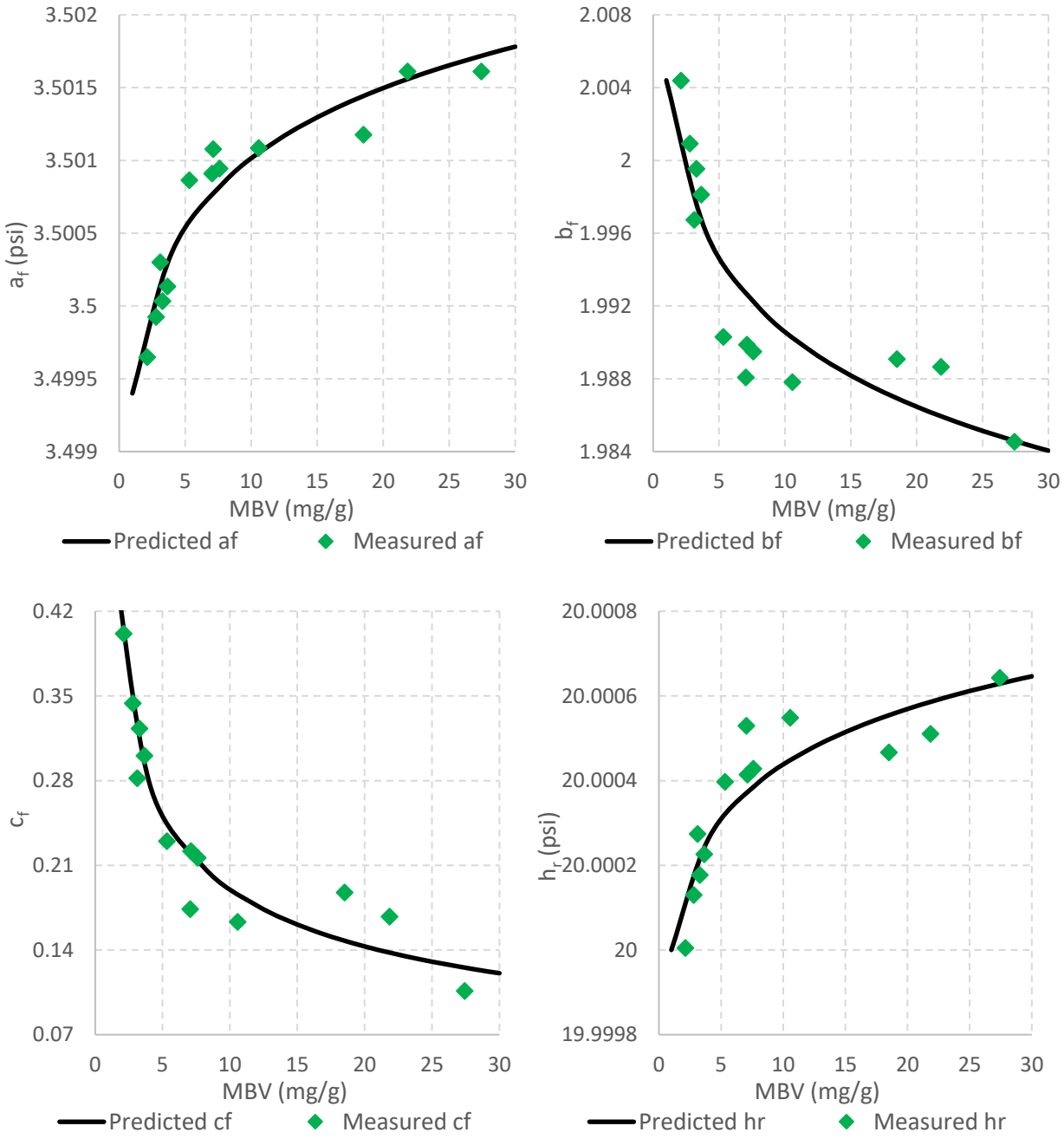

Figure 10. Change in a_f, b_f, c_f, and h_r with respect to the Methylene Blue Value

4.6. Suction Dielectric Characteristics Curve (SDCC) Prediction Model

The dielectric constant of base course aggregate can be directly used to determine soil suction using the Suction Dielectric Characteristic Curve (SDCC). In this study, a mathematical model based on the approach proposed by Juarez-Badillo was utilized to generate the Suction Dielectric Characteristic Curve (SDCC) [45]. This model is founded on the philosophical principle that changes in the dielectric constant, within

defined boundary limits, correspond to changes in soil suction, which ranges from zero suction to a maximum value of 10^6 kPa. The general form of the Suction Dielectric Characteristic Curve is presented in Equation 20.

$$\varepsilon_r = \left[\frac{\varepsilon_{sat} + \varepsilon_{\min} \alpha \left[\frac{h}{1x10^6 - h} \right]^{\gamma}}{1 + \alpha \left(\frac{h}{1x106 - h} \right)^{\gamma}} \right] \tag{20}$$

where ε_{sat} is the saturated dielectric value, ε_r is the soil dielectric value, ε_{min} is the minimum dielectric constant, h is the suction value (kPa), α and γ are the fitting parameters that change with the soil characteristics. A detailed derivation of the SDCC model, along with the boundary conditions for the defined functions, can be found in a previously published article [33]. Figure 11 illustrates a typical SDCC for base material, representing the relationship between matric suction (h) and the dielectric constant (ε_r) as described by Equation 20.

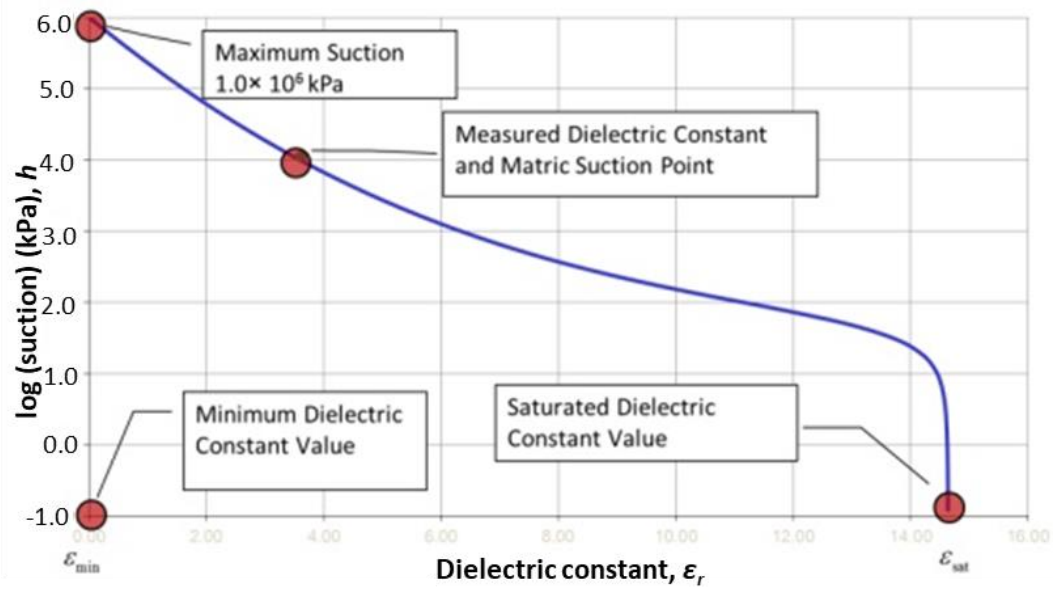

Figure 11. A Typical SDCC of base materials

Here, the minimum dielectric constant (ε_{min}) can be calculated using Equation 21.

$$\sqrt{\varepsilon_{\min}} = 1 + \theta_s (\sqrt{\varepsilon_{sat}} - 1) \tag{21}$$

where, θ_s is the volumetric solid content.

As shown in Figure 11, SDCC is an S-shaped curve and requires the input of the saturated dielectric constant (ε_{sat}), suction (h), and two fitting parameters (α, γ). These two fitting parameters primarily govern the change in the shape of the SDCC. In this study, an efficient methodology has been developed to determine the parameters α, γ, and ε_{sat} based on MBV and pfc values. Regression analysis was performed using the JMP statistical software program to investigate the correlation between the identified fitting parameters and the MBV, pfc value. Two distinct sets of α and γ parameters were defined based on the MBV value conditions: MBV less than 7.0 mg/g and MBV greater than 7.0 mg/g. For a MBV of less than 7.0 mg/g, the prediction equations for α and γ parameters are presented in Equations 22 and 23.

$$\alpha = 3.976 * (pfc * MBV)^{0.0015} \quad (22)$$

$$\gamma = -4E-08 * (pfc * MBV)^2 + 4E-07 * (pfc * MBV) + 0.0301 \quad (23)$$

Similarly, with a MBV greater than 7.00 mg/g, the equations for α and γ are expressed in Equations 24 and 25.

$$\alpha = 3.9649 * (MBV)^{0.0054} \quad (24)$$

$$\gamma = 0.0683 * (MBV)^{-0.102} \quad (25)$$

The saturated dielectric constant, ε_{sat}, is also dependent on MBV and can be represented by a simple second-order polynomial expression, as shown in Equation 26

$$\varepsilon_{sat} = 0.0334(MBV^2) - 0.1086(MBV) + 12.569 \quad (26)$$

Figure 12 presents the comparison of the predicted parameters based on Equation 22-25 and the measured values.

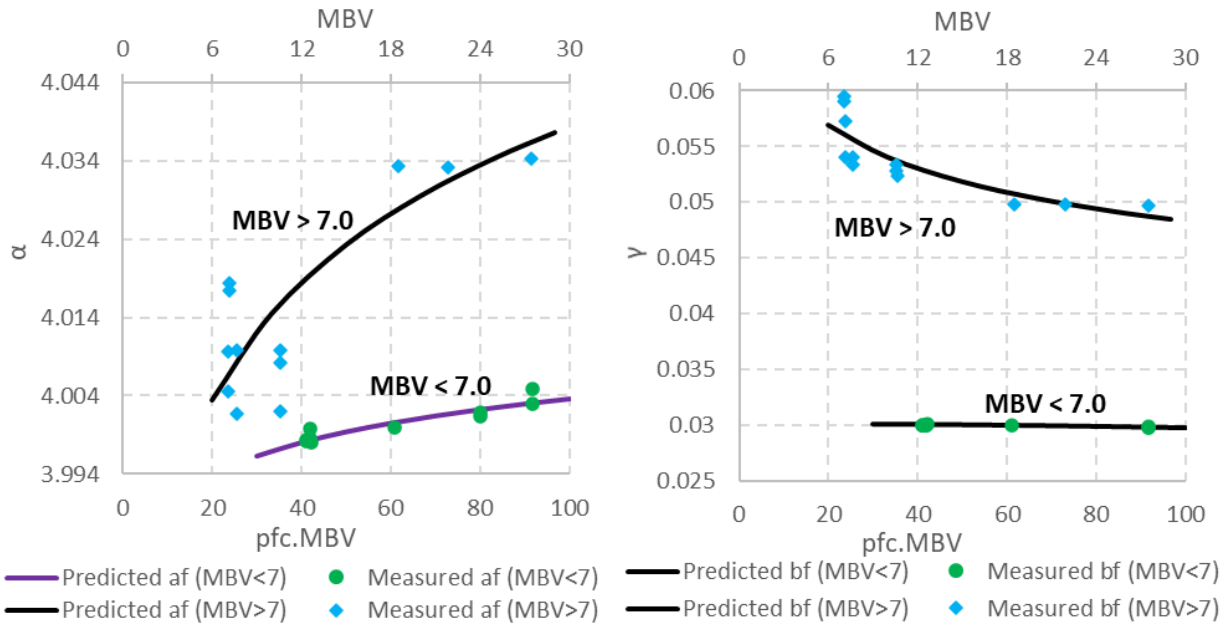

(a) (b)

Figure 12. Correlation of (a) α, and (b) γ parameters with *pfc* and MBV

4.7. Compaction Curve Prediction Model

To investigate the moisture-density relationship in compacted soil samples, a new mathematical model known as the compaction curve model (CCM) was utilized. The typical shape of a compaction curve is generally a C-shaped curve. Therefore, this model was derived by adapting the general form of a C-shaped equation, which is a common mathematical model for specific energy used in fluid mechanics, to the mathematical representation of the dry unit weight in unsaturated conditions [44, 46]. The equation for dry unit weight in an unsaturated condition is presented as follows.

$$\frac{\gamma_d}{\gamma_w} = \frac{1}{\frac{\theta_w}{\theta_s}+\frac{1}{G_s}} \tag{27}$$

where, γ_d is the dry unit weight of base material, γ_w is the unit weight of water, θ_w is the volumetric water content, θ_s is the saturated volumetric water content, and G_s is the specific gravity of the solids. The modified model consists of three parameters (a_d, b_d, and n_d) that vary with aggregate sources and characteristics. The mathematical formulation of the modified dry unit weight model is expressed as follows

$$\frac{\gamma_d}{\gamma_w} = [\frac{a_d}{(\frac{\theta_w}{\theta_s} + \frac{1}{G_s})^{n_d}} - \frac{b_d}{(\frac{\theta_w}{\theta_s} + \frac{1}{G_s})}] \quad (28)$$

To compare the accuracy of the modified compaction curve model, laboratory compaction tests were conducted for various aggregate sources. In order to generate the full compaction curve, dry unit weights are measured at four different moisture contents for aggregate sources. The modeled CCM follows a very similar pattern to that which the experimental compaction curve follows. The three parameters (a_d, b_d, and n_d) in the developed compaction model is identified using a least square minimum error curve fitting with the laboratory test results.

Furthermore, the relationship between unbound aggregate material properties and the estimated fitting parameters are investigated by JMP program. The parameters a_d, b_d, and n_d were found to be highly dependent to *pfc*, MBV, and G_s as expressed in Equation 29-31.

$$a_d = -0.725 * MBV + 0.239 * pfc + 0.878 * G_S + 1.88 \quad (29)$$

$$b_d = 0.108 * MBV - 0.167 * pfc + 0.160 * G_S + 0.122 \quad (30)$$

$$n_d = -0.013 * MBV - 0.045 * pfc + 0.013 * G_S + 0.058 \quad (31)$$

Figure 13 shows a comparison between measured and predicted coefficient values based on simple aggregate properties.

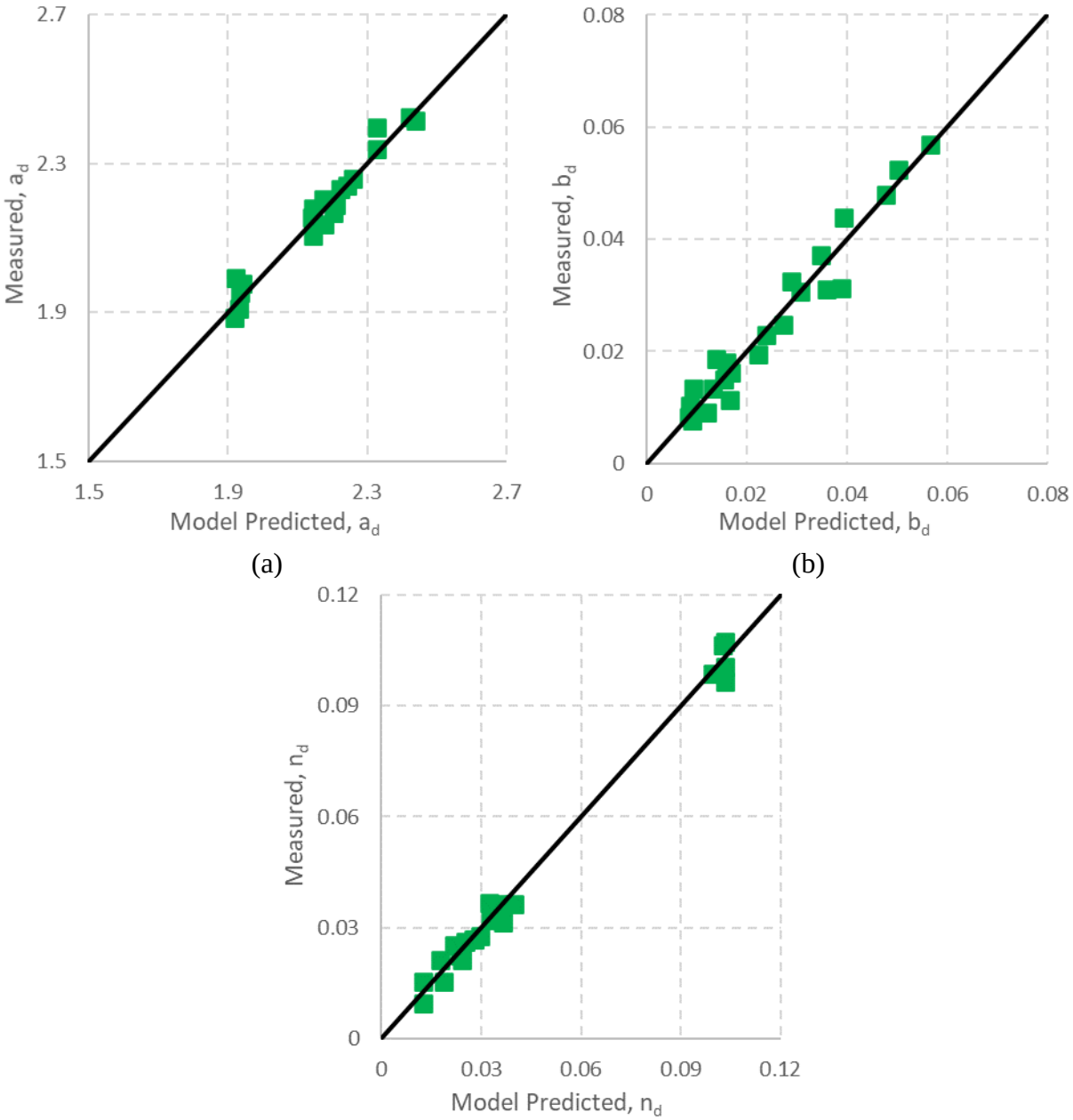

Figure 13. Comparison of measured versus model predicted CCM parameters, (a) a_d, (b) b_d, and (c) n_d, using regression models

4.8. Resilient Modulus (M_R) Prediction model

In order to predict the *k*-values in the resilient modulus model, as expressed in Equation 11, the M_R-tests were conducted for aggregate specimens collected from various sources. Using the test results at different loading sequences and moisture contents, the M_R model parameters were estimated for each source of base

materials by conducting a least square error curve fitting method. The k_1 , k_2, and k_3 parameters in the M_R model are influenced by the performance-related properties of unbound base materials. A Multiple regression analysis was performed using the JMP software to investigate the correlation between the *k* values and the base properties, including the dry density (γ_d), gravimetric water content (θ_g), MBV, pfc, and aggregate gradation (*G*), angularity (*A*), shape (*S*), and texture (*T*) in terms of the shape parameter, a, and the scale parameter, λ, in the Weibull distribution function. It was found that γ_d, shape (*S*), angularity (*A*), and texture (*T*) parameters and *pfc* are significant variables in the prediction models. A detailed discussion of the development of correlations models, along with results of the regression analysis, was provided in Gu et al. (2015). Equations 32 to 34 present the prediction models for k_1 , k_2, and k_3, respectively, derived from the regression analysis.

$$ln\, k_1 = -137.19 + 13.60\, ln(\gamma_d) + 4.35\, ln(\lambda_A) - 0.62\lambda_S + 1.68\, ln(\lambda_T) \quad (32)$$

$$k_2 = 36.14 + 0.04\,\mathrm{pfc} - 3.81\ln(\lambda_A) - 0.22\,a_S - 0.77\ln(\lambda_T) \quad (33)$$

$$k_3 = -4.39 + 0.45\ln(\gamma_d) - 0.01\,\mathrm{pfc} + 0.05\,a_S + 0.15\ln(\lambda_T) \quad (34)$$

Figure 14 compares the ***k*** values predicted by Equations. 32–34 with those measured using test results. Overall, the k values predicted using the correlation models produced a good fit with the measured values, depicting an R^2 value above 0.9. This indicates that the proposed easily available base material properties can accurately predict the *k* parameters in the M_R model.

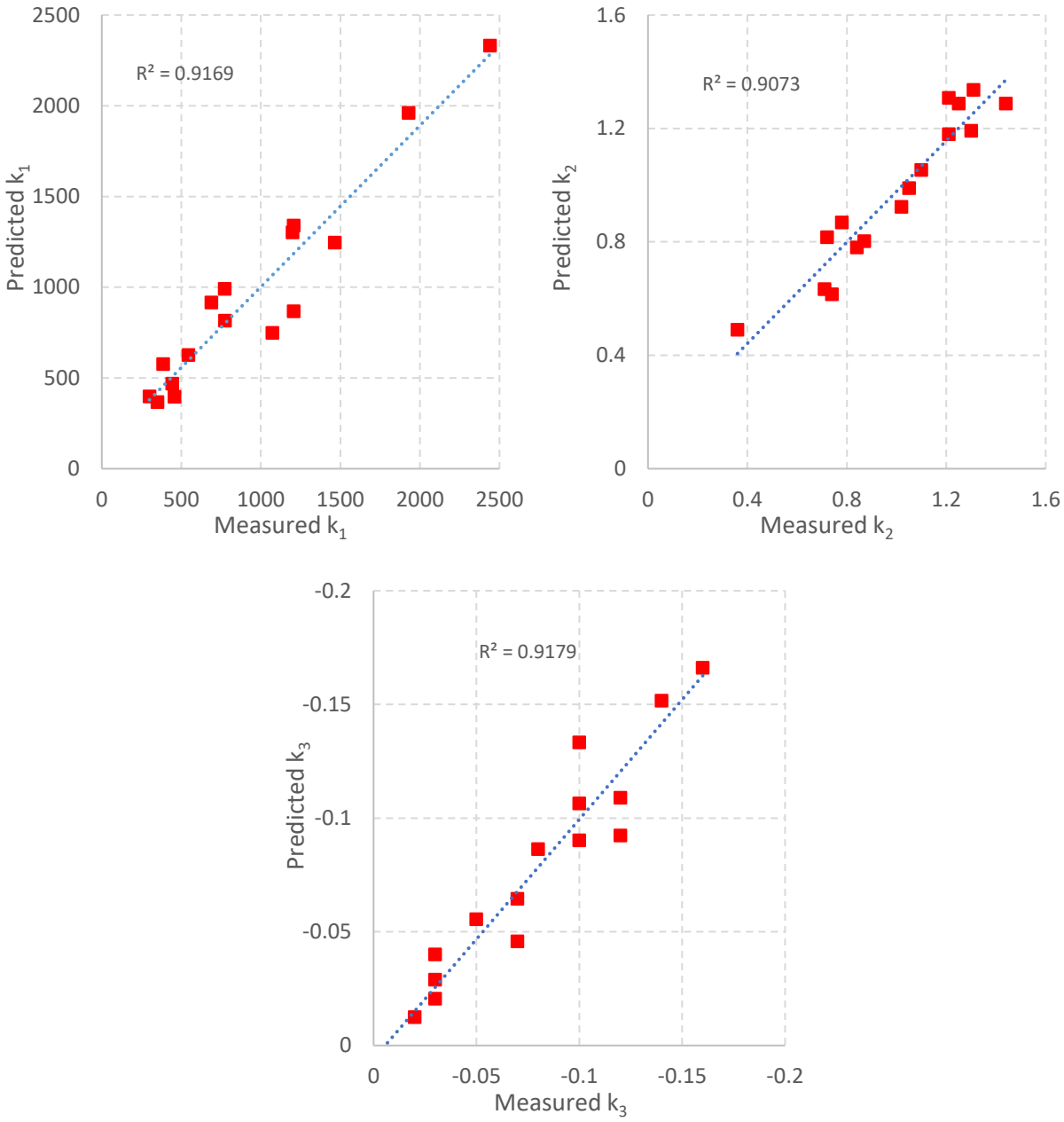

Figure 14. Comparison of measured versus predicted *k*-values using regression models based on performance-related material properties

4. Validation

To validate the prediction accuracy of the developed correlation models (i.e., SWCC fitting parameters, SDCC fitting parameters, CCM parameters, M_R-model parameters), we compared the predicted characteristics curves (SWCC, SDCC, CCM) and M_R-values of aggregate materials from nine selected queries with those measured using the laboratory tests results.

The accuracy of the proposed SWCC fitting parameter correlation models was evaluated by comparing the generated SWCCs using the predicted parameters with the measured matric suction values obtained from the filter paper test. Each SWCC was generated by entering the predicted fitting parameters (a_f, b_f, c_f, and h_r) into Equations 14 and 15. Figure 15 shows that the model-predicted SWCCs are in good agreement with the measured matric suction values from the filter paper test. This indicates that the SWCC fitting parameters for aggregate base materials can be reliably predicted based on the MBV.

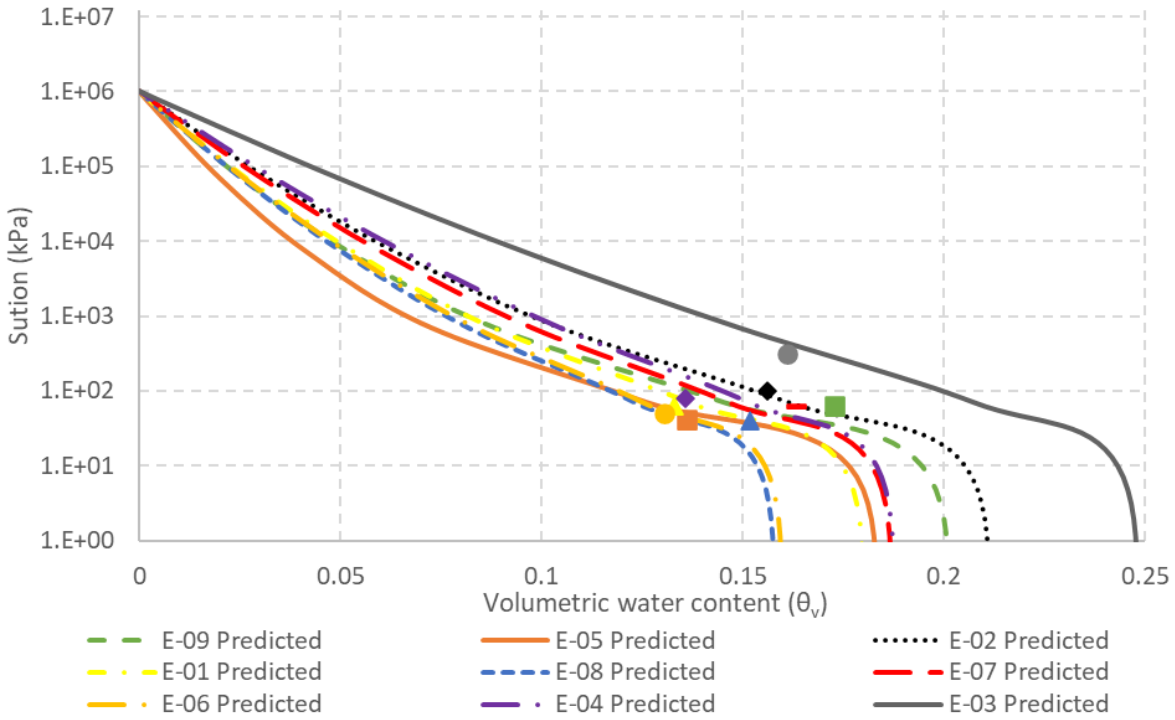

Figure 15. Comparison of predicted SWCC curves versus measured suction values for selected base materials

Similarly, Figure 16 illustrates a family of generated SDCCs with respect to the dielectric constant values for the nine selected aggregate pits. The three predicted parameters ε_{sat}, α, and γ were substituted into Equation 20 to obtain the SDCC for entire suction range. To validate the predicted curves, the experimentally measured suction and dielectric constant values for the same set of aggregate samples were plotted in Figure 16. The strong match between the predicted SDCCs and the measured suction-dielectric constant relationships establishes that the developed SDCC parameter prediction models can be reliably

utilized to generate the SDCC for base aggregate materials and to determine suction values from dielectric constant readings, as presented in Figure 2.

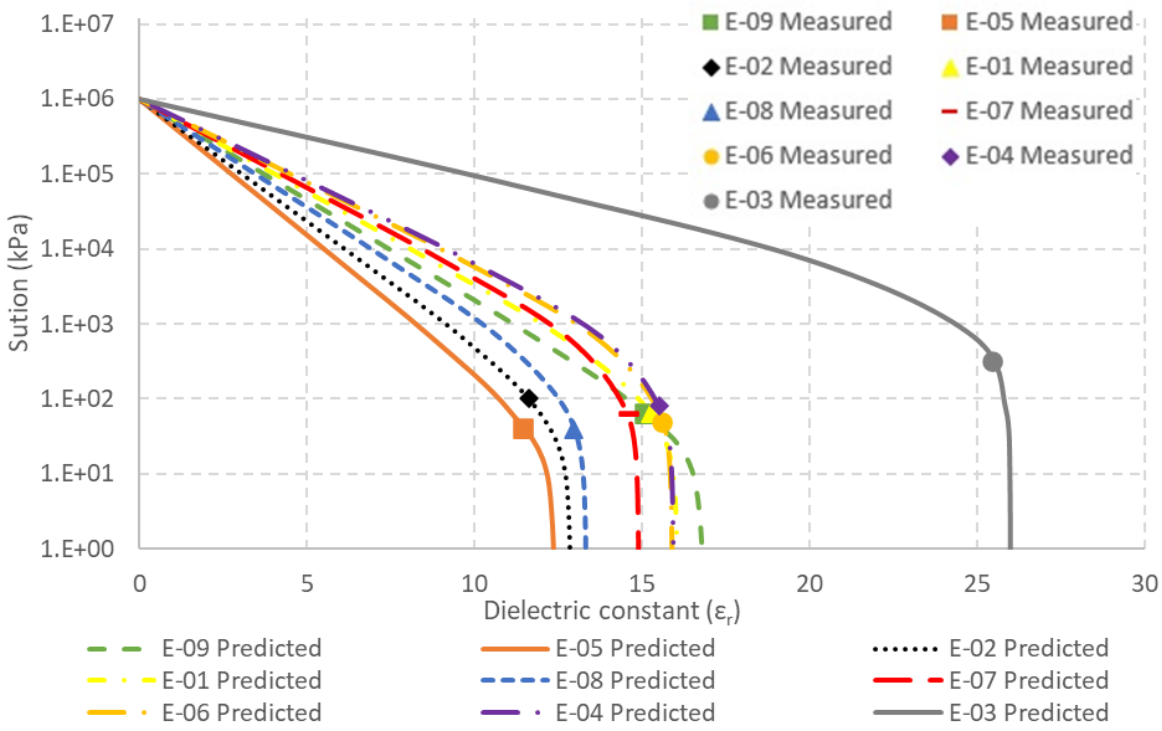

Figure 16. Comparison of predicted SDCC curves versus measured suction-dielectric constant values for selected base materials

To validate the accuracy of the proposed CCM fitting parameter prediction models, the laboratory-measured compaction curves and the predicted compaction curves were plotted together for the same aggregate samples. Figure 17 shows that the predicted CCM follows a similar pattern to the experimental compaction curve. It is also noted that the five calculated points using the CCM model align closely with the corresponding experimental measurements. The minimum density difference between the two curves occurs at the maximum dry density point. Therefore, it can be concluded that the proposed CCM, derived using the a_d, b_d, and n_d parameter prediction models, can effectively predict the relationship between gravimetric water content and dry density for base materials.

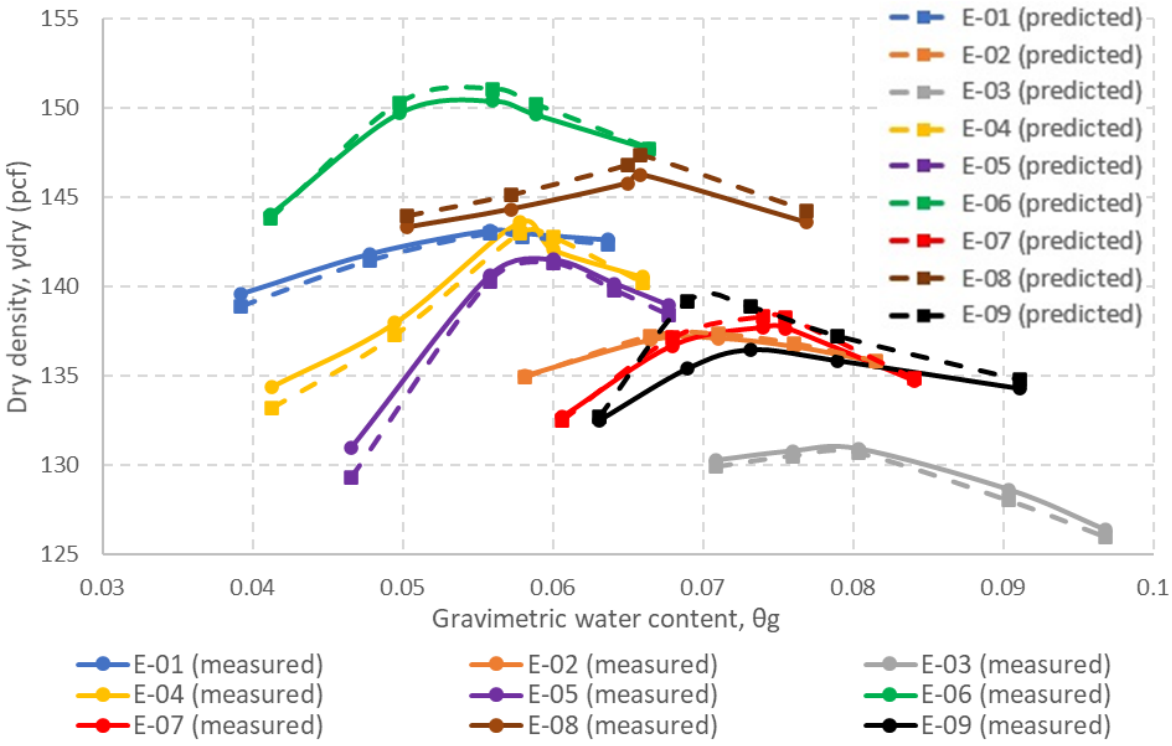

Figure 17. Comparison of CCM predicted and lab-measured compaction curves

The accuracy of predicted M_R values is examined for the collected base materials. The predicted k_1 , k_2, and k_3 coefficients from the three regression models were input into Equation 11 to calculate M_R values, which were then compared with the measured M_R test results. Figure 18 presents the comparisons between measured and predicted M_R values. The results clearly show that the M_R values estimated using the coefficient models, based on performance-related base properties, matched well with the test data. The estimated R^2 value of 0.63 indicates a relatively good accuracy, suggesting that the proposed coefficient models can effectively predict the M_R-value of base materials.

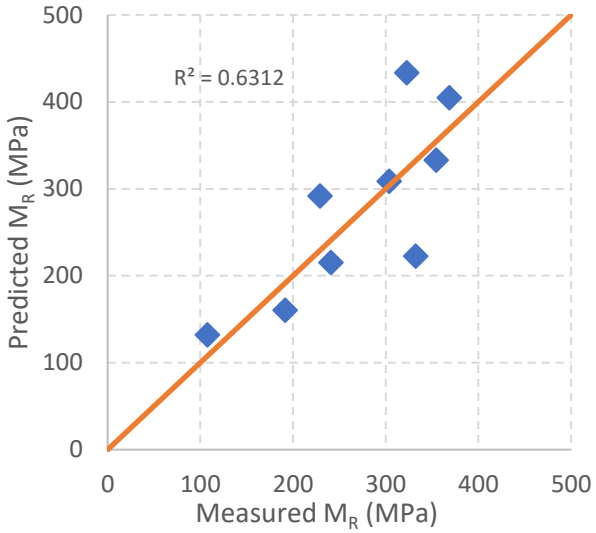

Figure 18. Comparison of model predicted resilient moduli against lab-measured values

Therefore, applying the measured dielectric constant value to the suction-dielectric characteristic curve (SDCC) yields the corresponding suction value for aggregate materials. This suction value can be used on the SWCC to determine the water content at that condition. Subsequently, the dry-density of the aggregate is determined using the predicted water content from the SWCC applied to the CCM. For example, a known dielectric constant value of 9.46 for the E-06 base material corresponds to a suction value of 7244 kPa, as obtained from the SDCC curve. As shown in Figure 15, the water content for E-06 at this suction value is 0.062. The dielectric constant value of base materials can be measured either in the laboratory using a Percometer or in the field with a GPR device, as described in the next section.

Field Validation

In this section, the GPR-based NDT approach was employed to evaluate the engineering properties of the base layer under field conditions, including h_m, θ_v, γ_d, and M_R, using the developed characteristics curve models. Figure 2 illustrates the procedures for implementing the GPR based monitoring approach to estimate the base properties for field projects. The GPR outputs were initially analyzed using the Pavecheck software to obtain the dielectric constant profile of base layer. The laboratory characterization test results, along with the dielectric constant data, were then input into the LayerMAPP software to estimate the in-situ properties of base materials. In order to validate the predicted h_m values from the GPR approach, core samples of the base were extracted for laboratory analysis. The predicted θ_v, γ_d, and M_R values of the base

layers were compared with those obtained from the NDG measurements and back-calculated from the FWD test data, respectively. In this study, GPR scan data were obtained from two different pavement sections in Texas during construction, as collected by the Texas Department of Transportation. These sections are identified as State Highway-24 (SH-24) and Farm to Market Road-159 (FM-159), located in Delta and Brazos Counties, respectively (Figure 19a). A summary of pavement layer thickness and the pavement layer types is presented in Figure 19b.

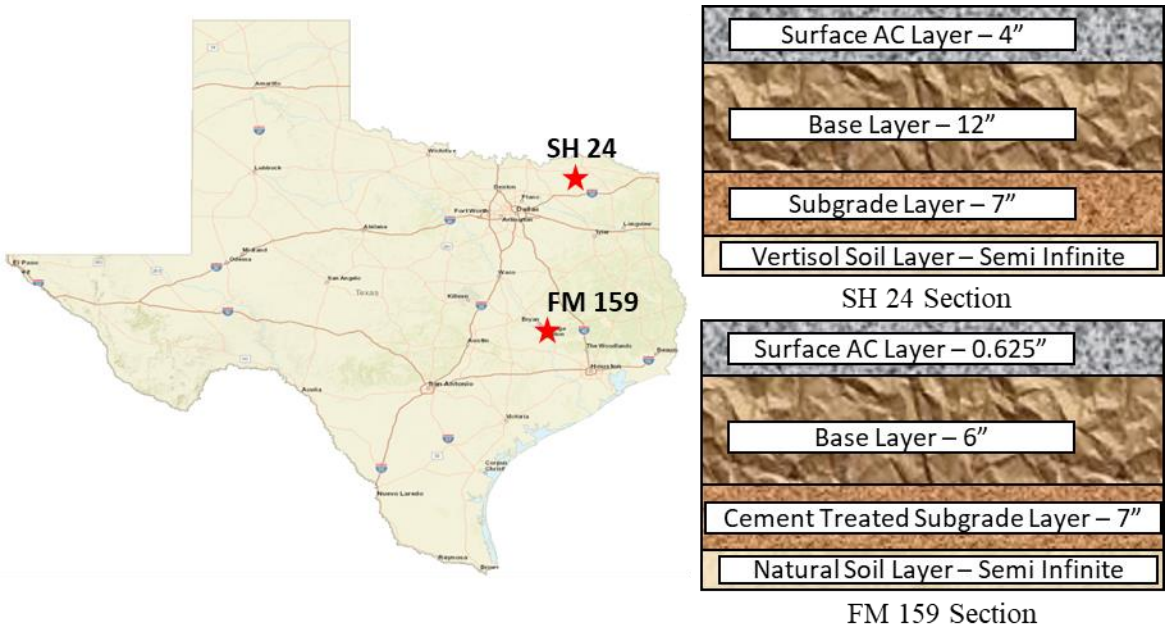

(a) (b)

Figure 19. (a) Location of SH-24 and FM-159 pavements in Texas (ArcGIS map); (b) illustration of SH-24 and FM-159 pavements structure

SH-24, Cooper Town – Delta County, TX

The GPR data analyzed in this pavement section was collected over a length of 4.5 miles from the westbound lane of the construction site. The scanning was performed on a newly constructed pavement using an air-coupled GPR system mounted on a van. Three core samples were extracted from selected locations within the pavement for laboratory characterization and to validate the predicted properties of the base layer. The base course material for SH-24 was primarily sandstone. According to the test results, the plasticity index ranged around 3.2, with an optimum moisture content of 6.9% and a maximum dry density of 137.3 lb/ft^3. Additional parameters measured in the laboratory included the MBV, which was 7.2, and

the PFC, which was 9%. These values were utilized to generate the characteristic curves for the SH-24 base material.

The GPR scan data were imported into the PaveCheck program for processing. A detailed description instructions to use PaveCheck software program can be found in PaveCheck user manual [47]. The PaveCheck program generates a strip map of the layer thickness and dielectric constant of the base layer from the scan data. The thickness and dielectric constant data were further processed using the LayerMAPP software in the following order: (a) dielectric constant measurements were input to estimate the matric suction and water content of base layer based on the generated SDCC and SWCC; (b) the water content values were applied to the CCM to generate the dry density profile; and (c) the suction, water content and predicted k_1, k_2, and k_3 values were input into the FEM to calculate the resilient modulus profile of base layer based on the stress- and -water-content dependent M_R model. The predicted properties are turned into strip maps to display the variations along the length of the survey section. The outcomes of the analysis are presented in Figures 20a-20d. Figures 20a and 20b present the suction and volumetric water content profiles of the base layer in the SH-24 pavement section. The two locations marked in red correspond to the laboratory measurements of suction and volumetric water content values obtained from the collected cores. Both figures compare the calculated moving average values of suction and volumetric water content profile obtained from GPR scans with the measured values at specific locations. Overall, the calculated suction and water content values agree well with the measured values. Figure 20c presents the dry density values along the length of the survey section. To validate the dry density profile from LayerMAPP software, Nuclear Density Gauge readings were taken from the top of the base layer during construction. It is noted from Figure 20c that the measured dry density values from Nuclear Gauge are slightly lower than the calculated weighted average dry density profile obtained from the GPR scans. Figure 20d compares the GPR predicted resilient moduli of base layer with those backcalculated from FWD data. Overall, the model predictions agree well with the backcalculated results, with only one outlier point showing a higher modulus from the FWD compared to that calculated by LayerMAPP. The generated modulus profile in Figure 20d clearly shows the fluctuation and variation in the as-built resilient modulus of base layer. Therefore, the

GPR approach facilitates the comparison of the design modulus against the constructed layer modulus for each spot location.

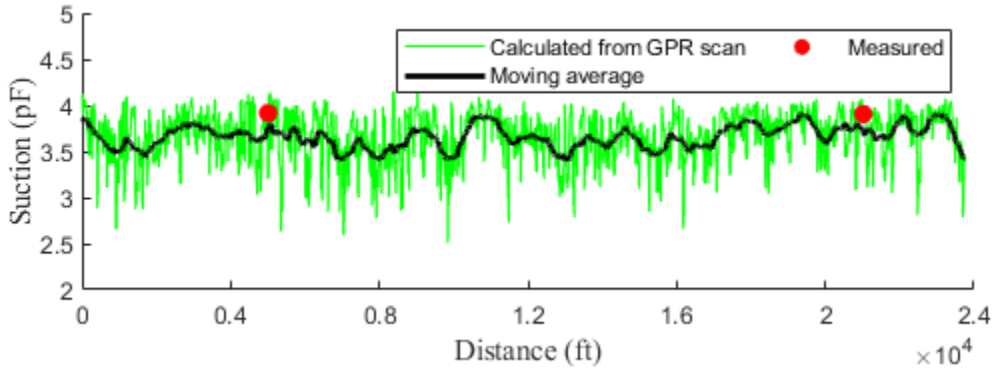

(a) Suction profile of the SH-24 test site

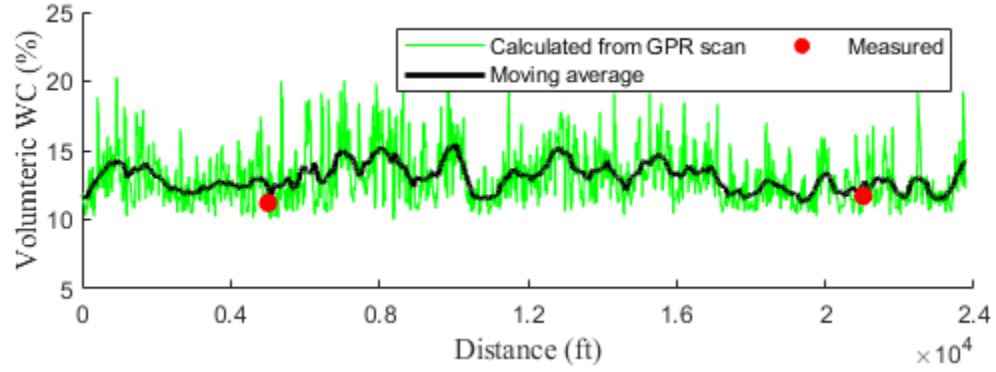

(b) Volumetric water content profile of the SH-24 test site

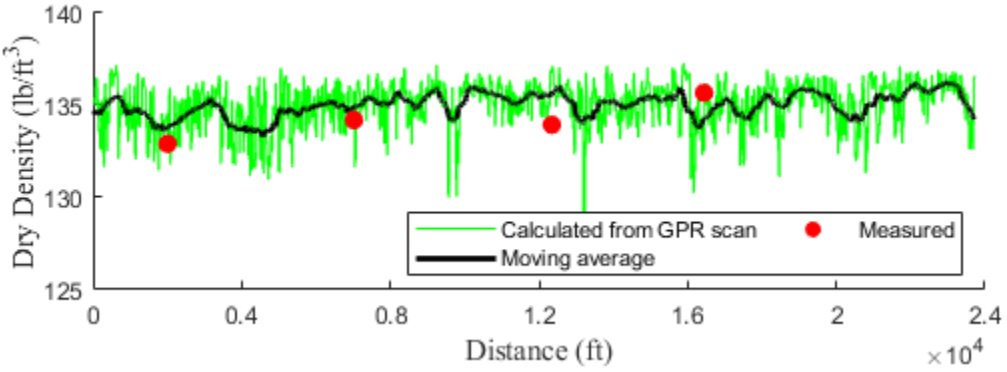

(c) Dry density profile of the SH-24 test site

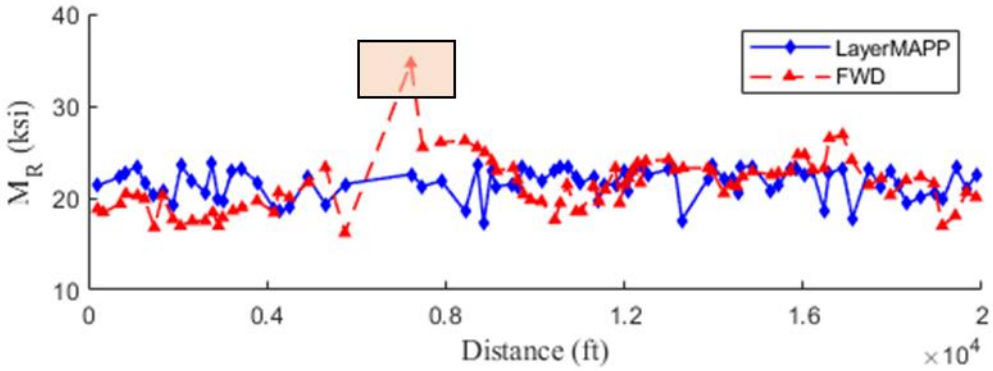

(d) Resilient modulus profile of the SH-24 test site

Figure 20. Generated profiles of (a) suction, (b) volumetric water content, (c) dry density, and (d) resilient modulus based on GPR scan data on SH-24 test site

FM-159, Bryan District – Brazos County, TX

Similarly, GPR field scans were conducted on the FM-159 asphalt pavement located in the Bryan district of Brazos County. Data was collected using an air-coupled GSSI 2 GHz Horn Antenna system over a 1,600-foot section. Simple laboratory tests were performed on the collected base materials to generate the necessary characteristics curves. The FM-159 base materials had a MBV of 4.5 and a *pfc* value of 9.5%. In order to compare the properties of the base layer predicted using the GPR approach, Nuclear Density Gauge measurements were collected from the surface of the base layer during construction. These measurements were collected at four different locations, which are indicated by red dot marks in Figures 21a and 21b. Overall, the dry density and water content values were in good agreement between the LayerMAPP calculations and the Nuclear Density Gauge measurements. As shown in Figure 21a, at the third test location, the difference between the water content values from the LayerMAPP calculations and the Nuclear Gauge is a maximum of 1.4%. Figure 21c compares the M_R-values predicted using GPR and the FWD. The center portion of the scanned section reveals the largest discrepancy between the predictions from GPR and those backcalculated from FWD, with an unreasonably low modulus value from FWD ranging between 10-15 ksi.

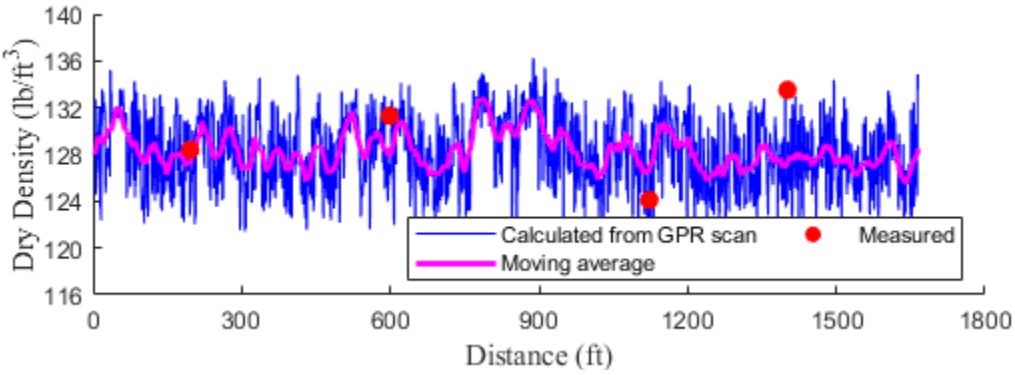

(a) Dry density of the FM-159 test site

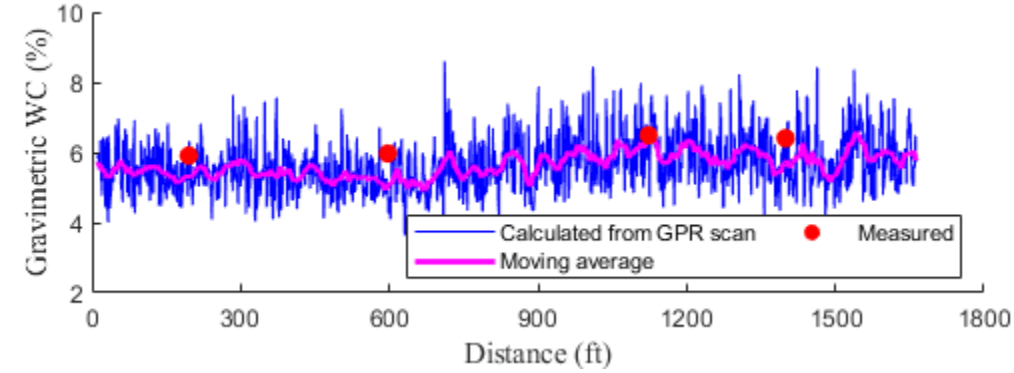

(b) Gravimetric water content of the FM-159 test site

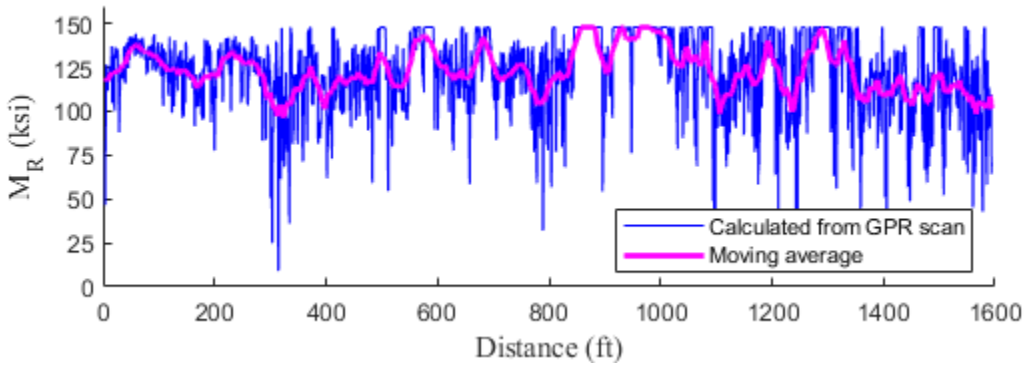

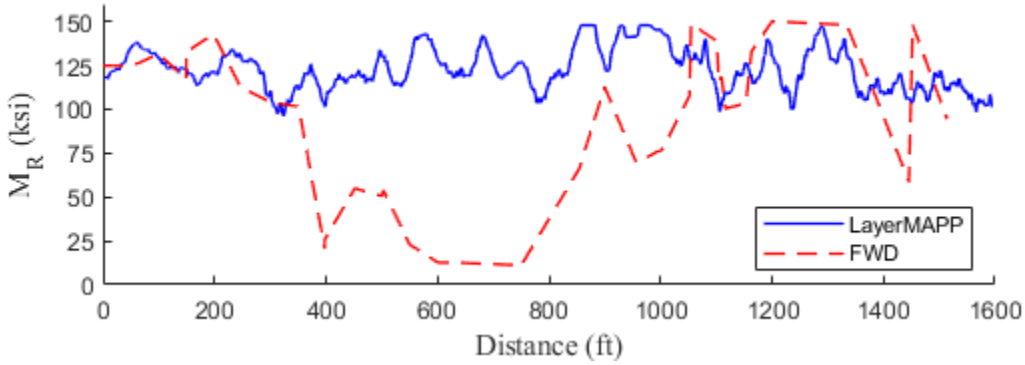

(c) Resilient Modulus of the FM-159 test site

Figure 21. Generated profiles of (a) volumetric water content, (b) dry density, and (c) resilient modulus based on GPR scan data on FM-159 test site

6. Conclusions and Recommendations

This study presents a quick, accurate and non-destructive method for determining important base material properties, i.e., suction, water content, dry density, and resilient modulus values using ground penetrating radar (GPR) readings and easily accessible laboratory characterization test results. The knowledge of base layer properties is important, especially in the construction phase, as accurate in-place layer properties can be used precisely to control the quality while the construction is underway. Additionally, these properties can be useful after the construction phase, as they can be fed into pavement management systems to predict pavement performance and rehabilitation priorities.

It has been observed that the engineering properties of the base layer fluctuate along the survey section. For instance, changes in dry density and resilient modulus of the base layers can be easily identified using the strip map generated from GPR scan readings. Poorly compacted locations are also detectable from this strip map. A detailed dry unit weight strip map of the SH-24 pavement section is illustrated in Figure 22. The figure highlights the locations where the dry density is significantly lower than the maximum dry density of 137.3 lb/ft^3. Therefore, if a spot or area is poorly compacted and falls below the minimum acceptable density limit, this can be instantly identified and rectified to an acceptable limit before placing a surface layer.

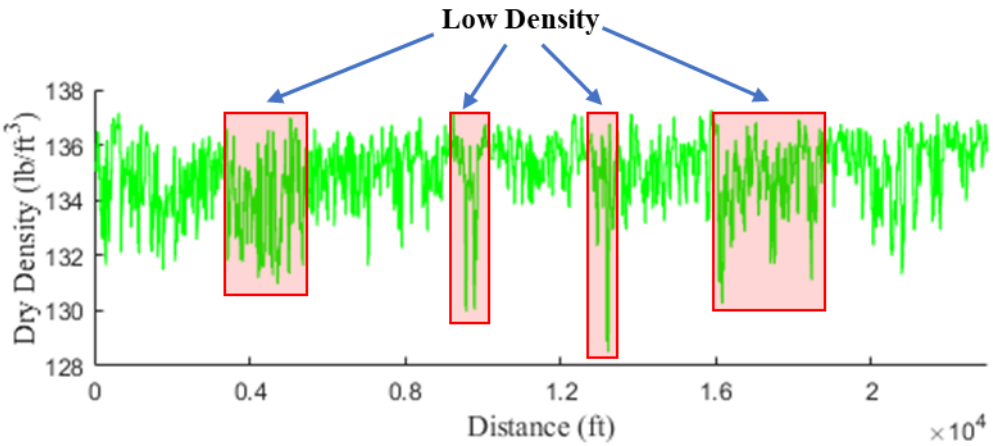

Figure 22. Highlighting the low-density Spots based on GPR measurements

Currently, nuclear density gauges (NDG) have been used by many agencies to evaluate the dry density of the pavement layers as a final compaction control device. The GPR method can be used as an effective compaction control method to determine the dry density using only the dielectric constant and the simple laboratory test values. In addition to the limited data that NDGs can provide from specific spot locations, it has also been known that the accuracy of the readings by NDG may be offset when the base aggregate materials contain fly ash, coal, clays, gypsum, lime, phosphates, and organic materials, which contain neutron or bound hydrogen. For example, gypsum, which includes water molecules in its crystalline structure, can lead to falsely high-water content readings from NDGs, resulting in inaccurately low dry density readings. However, there are no such limitations associated with either the GPR method. Furthermore, the modulus strip map generated using the GPR methodology allows for comparison between the predicted layer modulus along the construction section with the design modulus. This method takes into account variations in suction and water content measurements along the section, which result in a change in resilient modulus value.

In conclusion, the developed approach can be employed in both construction quality control and quality management processes, as it allows real-time assessment of all layer properties. The GPR approach also enables one to visualize the results as a strip map (color map), presenting the findings graphically, digitally, and clearly. The color map clearly presents higher and lower modulus subsections, aiding in decision making. One major concern for highways is the continuation of traffic flow without delays due to construction work. This challenge can be addressed through continuous monitoring of highway infrastructure and providing timely maintenance and rehabilitation for pavement structures. Nondestructive devices like GPR can facilitate this by offering real-time condition assessments of pavement structures at highway speeds. Efficient maintenance and rehabilitation efforts can ultimately reduce fuel consumption, traffic delays, and travel times.

The findings of this study emphasize the need for further research to improve this approach for better quality control and quality assurance of base sections. The existing version of the LayerMAPP software requires laboratory test data on aggregates properties, i.e., MBV, *pfc*, and aggregate size and shape characteristics

for the selected pavement sections to be analyzed. Given that the properties of some aggregate materials have similarities to others, it may be possible to apply the properties of a specific aggregate type that has similar characteristics to the new quarry. Hence, it will be helpful to develop an aggregate property dataset based on mineralogical and gradation classifications so that they can be directly utilized for aggregate material from a new source.

CRediT authorship contribution statement

Sajib Saha: Conceptualization, Data curation, Formal analysis, Methodology, Software, Validation, Visualization, Writing – original draft, review and editing. **Hakan Sahin:** Conceptualization, Data curation, Software, Visualization, Writing – original draft. **Narain Hariharan:** Conceptualization, Methodology, Writing – review and editing. **Bjorn Birgisson:** Supervision, Writing – review and editing. **Robert L. Lytton:** Formal analysis, Funding acquisition, Project administration, Supervision, Writing – review and editing.

Acknowledgements

This work was supported by the Texas Department of Transportation under Grant 0-6874 and 0-6621. The results in this article were based on tasks conducted in cooperation with the Texas A&M Transportation Institute, the Texas Department of Transportation, and the Federal Highway Administration. The authors would like to acknowledge the assistance provided by many individuals including Arvind Devadas and Dr. Yong Deng.

Declaration of interests

The authors declare that they have no known competing financial interests or personal relationships that could have appeared to influence the work reported in this paper.

Data availability

Data will be made available on request.

References

[1] Huang, Y. H. (2004). Pavement analysis and design (Vol. 2, pp. 401-409). Upper Saddle River, NJ: Pearson Prentice Hall.

[2] Annan, A. P. (2003). Ground Penetrating Radar: Principles, Procedures & Applications. Canada: Sensors & Software Incorporated.

[3] Zhao, S., Al-Qadi, I. L., & Wang, S. (2018). Prediction of thin asphalt concrete overlay thickness and density using nonlinear optimization of GPR data. NDT & E International, 100, 20-30.

[4] Lai, W. L., Kou, S. C., Tsang, W. F., & Poon, C. S. (2009). Characterization of concrete properties from dielectric properties using ground penetrating radar. Cement and Concrete Research, 39(8), 687-695.

[5] Khakiev, Z., Shapovalov, V., Kruglikov, A., Morozov, A., & Yavna, V. (2014). Investigation of long term moisture changes in trackbeds using GPR. Journal of Applied Geophysics, 110, 1-4.

[6] Tosti, F., Adabi, S., Pajewski, L., Schettini, G., & Benedetto, A. (2014, June). Large-scale analysis of dielectric and mechanical properties of pavement using GPR and LFWD. In Proceedings of the 15th International Conference on Ground Penetrating Radar (pp. 868-873). IEEE.

[7] Zhao, S., & Al-Qadi, I. L. (2016). Development of an analytic approach utilizing the extended common midpoint method to estimate asphalt pavement thickness with 3-D ground-penetrating radar. Ndt & E International, 78, 29-36.

[8] Shapovalov, V., Yavna, V., Kochur, A., Khakiev, Z., Sulavko, S., Daniel, P., & Kruglikov, A. (2020). Application of GPR for determining electrophysical properties of structural layers and materials. Journal of Applied Geophysics, 172, 103913.

[9] Liu, H., Yang, Z., Yue, Y., Meng, X., Liu, C., & Cui, J. (2023). Asphalt pavement characterization by GPR using an air-coupled antenna array. NDT & E International, 133, 102726.

[10] Zhang, J., Li, H., Yang, X., Cheng, Z., Zou, P. X., Gong, J., & Ye, M. (2024). A novel moisture damage detection method for asphalt pavement from GPR signal with CWT and CNN. NDT & E International, 145, 103116.

[11] Zhang, J., Lin, H., & Doolittle, J. (2014). Soil layering and preferential flow impacts on seasonal changes of GPR signals in two contrasting soils. Geoderma, 213, 560-569.

[12] Galagedara, L. W., Parkin, G. W., Redman, J. D., Von Bertoldi, P., & Endres, A. L. (2005). Field studies of the GPR ground wave method for estimating soil water content during irrigation and drainage. Journal of hydrology, 301(1-4), 182-197.

[13] Schmalz, B., & Lennartz, B. (2002). Analyses of soil water content variations and GPR attribute distributions. Journal of Hydrology, 267(3-4), 217-226.

[14] Benedetto, A. (2010). Water content evaluation in unsaturated soil using GPR signal analysis in the frequency domain. Journal of Applied Geophysics, 71(1), 26-35.

[15] Wang, P., Hu, Z., Zhao, Y., & Li, X. (2016). Experimental study of soil compaction effects on GPR signals. Journal of applied geophysics, 126, 128-137.

[16] Jaumann, S., & Roth, K. (2018). Soil hydraulic material properties and layered architecture from time-lapse GPR. Hydrology and Earth System Sciences, 22(4), 2551-2573.

[17] Zegeye-Teshale, E., Holzbauer, M., & Dai, S. (2022). Using Ground Penetrating Radar to Monitor Seasonal Moisture Fluctuations in Base Layers of Existing Roads. Transportation Research Record, 2676(6), 371-386.

[18] Wang, S., Zhao, S., & Al-Qadi, I. L. (2018). Continuous real-time monitoring of flexible pavement layer density and thickness using ground penetrating radar. Ndt & E International, 100, 48-54.

[19] Wang, S., Al-Qadi, I. L., & Cao, Q. (2020). Factors impacting monitoring asphalt pavement density by ground penetrating radar. Ndt & E International, 115, 102296.

[20] ASTM D 698. (2007). Standard Test Methods for Laboratory Compaction Characteristics of Soil Using Standard Effort (12 400 Ft-lbf/ft3 (600 KN-m/m3)) 1. ASTM Committee D-18 on Soil and Rock. ASTM International.

[21] ASTM D 5298. (2003). Standard test method for measurement of soil potential (suction) using filter paper. ASTM International.

[22] Bulut, R., Lytton, R. L., & Wray, W. K. (2001). Soil suction measurements by filter paper. In Expansive clay soils and vegetative influence on shallow foundations (pp. 243-261).

[23] Das, B. M. (2020). Principles of geotechnical engineering. 10th Edition.

[24] Daniel, D. E., & Benson, C. H. (1990). Water content-density criteria for compacted soil liners. Journal of Geotechnical Engineering, 116(12), 1811-1830.

[25] Yu, X., & Drnevich, V. P. (2004). Soil water content and dry density by time domain reflectometry. Journal of Geotechnical and Geoenvironmental Engineering, 130(9), 922-934.

[26] Tex-113-E. (2011). Texas Department of Transportation (TxDOT). Laboratory compaction characteristics and moisture-density relationships of base materials., Austin, TX.

[27] Gu, F., Sahin, H., Luo, X., Luo, R., & Lytton, R. L. (2015). Estimation of resilient modulus of unbound aggregates using performance-related base course properties. Journal of Materials in Civil Engineering, 27(6), 04014188.

[28] AASHTO T307-99. (2003). “Standard method of test for resilient modulus of subgrade soils and untreated base/subbase materials.” Washington, DC.

[29] Lytton, R. (1996). Foundations and pavements on unsaturated soils. Proceedings’. of the First International Conference on Unsaturated Soils, Unsat’95, Vol. 3, pp. 1201–1220, Paris, France.

[30] Yool, A. I. G., Lees, T. P., & Fried, A. (1998). Improvements to the methylene blue dye test for harmful clay in aggregates for concrete and mortar. Cement and concrete research, 28(10), 1417-1428.

[31] Nikolaides, A., Manthos, E., & Sarafidou, M. (2007). Sand equivalent and methylene blue value of aggregates for highway engineering. Foundations of civil and environmental engineering, 10, 111-121.

[32] Muñoz, J. F., Gullerud, K. J., Cramer, S. M., Tejedor, M. I., & Anderson, M. A. (2010). Effects of coarse aggregate coatings on concrete performance. Journal of Materials in Civil Engineering, 22(1), 96-103.

[33] Sahin, H. (2014). Nondestructive test methods for rapid assessment of flexible base performance in transportation infrastructures (Doctoral dissertation).

[34] Sahin, H., Gu, F., & Lytton, R. L. (2015). Development of soil-water characteristic curve for flexible base materials using the methylene blue test. Journal of Materials in Civil Engineering, 27(5), 04014175.

[35] Yeo, Y. S., Nikraz, H., & Jitsangiam, P. (2012). Tube suction test to measure moisture susceptibility of Australian pavements. Engineering journal, 16(4), 159-168

[36] Masad, E., & Fletcher, T. (2005). Aggregate imaging system (AIMS): Basics and applications (No. FHAWA/TX-05/5-1707-01-1). Texas Transportation Institute, Texas A & M University System.

[37] Montgomery, D. C., & Runger, G. C. (2010). Applied statistics and probability for engineers. John wiley & sons.

[38] Fredlund, D. G., & Xing, A. (1994). Equations for the soil-water characteristic curve. Canadian geotechnical journal, 31(4), 521-532.

[39] Zapata, C. E. (2010). A national database of subgrade soil-water characteristic curves and selected soil properties for use with the MEPDG (No. NCHRP Project 9-23A).

[40] Saha, S., Gu, F., Luo, X., & Lytton, R. L. (2017). Prediction of soil-water characteristic curve using artificial neural network approach. In PanAm Unsaturated Soils 2017 (pp. 124-134).

[41] Perera, Y. Y., Zapata, C. E., Houston, W. N., & Houston, S. L. (2005). Prediction of the soil-water characteristic curve based on grain-size-distribution and index properties. In Advances in pavement engineering (pp. 1-12).

[42] Torres-Hernandez, G. (2011). "Estimating the soil–water characteristic curve using grain size analysis and plasticity index." M.Sc. thesis, Arizona State Univ., Tempe, AZ.

[43] Saha, S., Gu, F., Luo, X., & Lytton, R. L. (2018). Prediction of soil-water characteristic curve for unbound material using Fredlund–Xing equation-based ANN approach. Journal of Materials in Civil Engineering, 30(5), 06018002.

[44] Epps, J., Sebesta, S., Hewes, B., Sahin, H., Luo, R., Button, J., ... & Gu, F. (2014). Development of a specification for flexible base construction (No. FHWA/TX-13/0-6621). Texas. Dept. of Transportation. Research and Technology Implementation Office.

[45] Juarez-Badillo, E. (1981). General compressibility equation for soils. In: Proc. Tenth International Conference on Soil Mechanics and Foundation Engineering. Stockholm, Sweden, pp. 171–178.

[46] Chaudhry, M. H. (2008). Open-channel flow (Vol. 523). New York: Springer.

[47] Liu, W., & Scullion, T. (2006). PAVECHECK: integrating deflection and ground penetrating radar data for pavement evaluation (No. FHWA/TX-06/0-4495-1).